

**Under-ice acoustic navigation using real-time model-aided range estimation**

EeShan C. Bhatt,<sup>1, 2, a</sup> Oscar Viquez,<sup>2</sup> and Henrik Schmidt<sup>2</sup>

<sup>1</sup>*MIT-WHOI Joint Program in Oceanography/Applied Ocean Science & Engineering,  
Cambridge and Woods Hole, MA, USA*

<sup>2</sup>*Department of Mechanical Engineering, Massachusetts Institute of Technology,  
Cambridge, MA*

(Dated: 21 February 2022)

1 The long baseline (LBL) underwater navigation paradigm relies on the conversion  
2 of recorded travel times into pseudoranges to trilaterate position. For real-time op-  
3 erations, this conversion has assumed an isovelocity sound speed. For re-navigation  
4 in post-processing, computationally and/or labor intensive acoustic modeling may  
5 be employed to reduce uncertainty driven by multipath arrivals. This work demon-  
6 strates a real-time ray-based prediction method of the effective sound speed along  
7 a path from source to receiver to minimize vehicle position error. This method was  
8 implemented for a small scale AUV-LBL system in March 2020, in the Beaufort Sea,  
9 in total ice-covered conditions and a double ducted acoustic propagation environ-  
10 ment. The vehicle was successfully deployed and recovered. Given the lack of GPS  
11 data throughout the vehicle’s mission, however, the pseudorange performance is first  
12 evaluated on connections between GPS-linked beacons. The real-time ranging error  
13 between beacons is roughly 11 meters at distances up to 3 km. But a consistent over-  
14 estimation in the real-time method provides insights for improved eigenray filtering  
15 by the number of surface bounces. An operationally equivalent pipeline is used to  
16 re-position the LBL beacons and re-navigate the AUV, using a modeled, historical,  
17 and a locally observed sound speed profile. The median re-navigation error is  $1.84 \pm 2.19$  RMS m. The improved trilateration performance for suggests that this ap-  
18 proach effectively extends the single meter accuracy of the deployed GNSS units into  
19 the water column.

---

<sup>a</sup>[ebhatt@whoi.edu](mailto:ebhatt@whoi.edu)

<sup>21</sup> **I. INTRODUCTION**

<sup>22</sup> Autonomous underwater vehicles (AUVs) are increasingly capable platforms to explore  
<sup>23</sup> and sample the ocean, particularly for remote and/or dangerous regions. However, navi-  
<sup>24</sup> gation uncertainty is a major challenge in considering AUVs as standard tools for oceano-  
<sup>25</sup> graphic research. While land and air-based robots utilize information from Global Naviga-  
<sup>26</sup> tion Satellite Systems (GNSS) to achieve stunning location accuracy and precision through-  
<sup>27</sup> out the duration of their missions, AUVs cannot access GNSS fixes while underwater. There-  
<sup>28</sup> fore, underwater vehicles have relied on any combination of dead reckoning, hydrodynamic  
<sup>29</sup> models, inertial navigation systems, doppler velocity logs, and acoustic baseline positioning  
<sup>30</sup> systems for navigation (Paull *et al.*, 2014). Limiting navigation error and drift requires an  
<sup>31</sup> AUV to periodically stall on the surface and obtain a GNSS fix to reset its position error.  
<sup>32</sup> This foolproof method of self-positioning is undesirable for stealth, adverse weather condi-  
<sup>33</sup> tions, and mission efficiency, and inaccessible in a GNSS-denied situation like an ice-covered  
<sup>34</sup> environment.

<sup>35</sup> Of underwater acoustic navigation systems, long baseline (LBL) is the most GPS-like  
<sup>36</sup> in style and scale, and most appropriate for mitigating drift without overburdening com-  
<sup>37</sup> putation or payload size on the vehicle (Van Uffelen, 2021). The state-of-the-art for LBL  
<sup>38</sup> outsources depth to a pressure sensor and solves the two-dimensional localization problem  
<sup>39</sup> with an isovelocity, linear scaling between one way travel time (OWTT) and range (Eustice  
<sup>40</sup> *et al.*, 2006, 2007; Webster *et al.*, 2009, 2012). This assumption is valid for short scale  
<sup>41</sup> operations but oversimplifies propagation for larger and/or complex acoustic environments.

42 To achieve single meter, GNSS-like performance in a GNSS-denied environment, we demon-  
 43 strate an embedded ray-based data processing algorithm to convert recorded OWTTs into  
 44 pseudorange estimates. This methodology was integrated onto the AUV *Macrura*, deployed  
 45 and recovered in the Beaufort Sea, in March 2020, during the Ice Exercise 2020 (ICEX20).  
 46 A physics-driven methodology that received an *in situ* sound speed profile (SSP) was nec-  
 47 essary despite the small operational domain because of the relatively high-risk mission en-  
 48 vironment—total under-ice conditions and a variable double ducted acoustic environment.  
 49 For consistency, we delineate specific definitions for timing, positioning, and navigation  
 50 from [Howe et al. \(2019\)](#).

- 51     1. Timing is the ability to acquire and maintain accurate and precise time anywhere in  
 52         the domain of interest within user-defined timeliness parameters
- 53     2. Positioning is the ability to accurately and precisely determine one's location refer-  
 54         enced to a standard geodetic system
- 55     3. Navigation is the ability to determine current and desired position (relative or absolute)  
 56         and apply corrections to course, orientation, and speed to attain a desired position  
 57         anywhere in the domain of concern

58 Thus, navigation is inherently in real-time and depends on positioning; positioning depends  
 59 on timing. We also suggest re-navigation and re-positioning as post-processed corollaries,  
 60 which may include knowledge or processing capabilities not available *in situ*.

61     While RAFOS floats championed one way ranging for re-positioning ([Duda et al., 2006](#);  
 62 [Rossby et al., 1986](#)), the ability to do so for navigation was facilitated by the advent of

63 the WHOI Micro-Modem (Singh *et al.*, 2006) and synchronized clocks (Rypkema *et al.*,  
64 2017). AUV navigation efforts have achieved root mean square (RMS) localization error on  
65 the order of tens of meters relative to GNSS surface position over less than ten kilometers  
66 in shallow (Claus *et al.*, 2018; Eustice *et al.*, 2007; Kepper *et al.*, 2017) and deep water  
67 (Jakuba *et al.*, 2008; Kunz *et al.*, 2008; Webster *et al.*, 2009). However, these efforts all used  
68 a nominal sound speed for travel time conversion and the vehicles were limited to shallower  
69 isovelocity regimes.

70 Localization algorithms that do consider environmental or acoustic uncertainty tend to  
71 focus on longer and larger experiments, where spatio-temporal variability cannot be ig-  
72 nored. These methods have also been reserved for post-processing as they can be labor  
73 intensive, computationally heavy, and/or require additional information like contemporane-  
74 ous data. For example, gliders navigating with kinematic flight models and equipped with  
75 acoustic modems were later unambiguously associated with predicted ray arrivals, resulting  
76 in roughly a kilometer error and hundred meters uncertainty over basin scale propagation  
77 (Van Uffelen *et al.*, 2013). A follow up study investigated how a single temporally and  
78 spatially averaged SSP could mitigate position error for a four month glider mission (Van  
79 Uffelen *et al.*, 2016). Wu *et al.* (2019) cross correlate three days of real acoustic records with  
80 synthetic ones generated through ocean model snapshots from HYCOM (Chassagnet *et al.*,  
81 2007). While potentially applicable for various ocean states, this is reliant on model realism  
82 and impractical for real-time operations. A “cold start” algorithm that does not require prior  
83 knowledge of track, position, or sound speed information inputs a four-dimensional ocean  
84 model, constrained by tomography data, into a range dependent ray code to isolate the last

85 path detected in a full multipath pattern (Mikhalevsky *et al.*, 2020). Then, a representative  
86 group speed is solved for alongside position in a least squares fashion. This approach is able  
87 to re-position a floating hydrophone array with an error of 58 m and a standard deviation  
88 of 32 m based on six sources 129–450 km away but remains to seen for real-time navigation.

89 The ICEX20 AUV deployment necessitated an environmentally- and physically-driven  
90 relationship between recorded travel times and estimated pseudoranges due to the multipath  
91 uncertainty brought upon by an increasingly observed double ducted environment in the  
92 Beaufort Sea, which some refer to as the “Beaufort Lens” (Chen *et al.*, 2019; Chen and  
93 Schmidt, 2020; Litvak, 2015).

94 Given that a lens introduces significant ray refraction, the Beaufort Lens is a shorthand for  
95 the spatio-temporal variability of the local temperature and sound speed maxima generally  
96 around 50 to 60 m in depth. A neutrally buoyant layer of warm Pacific Summer Water  
97 creates a unique double ducted environment —the upper duct degrades signal coherence  
98 due to intensified ice interaction and the lower duct effectively traps sound for long range  
99 propagation (Poulsen and Schmidt, 2017). Modeling output (Duda *et al.*, 2021, 2019) and  
100 experimental observations (Ballard *et al.*, 2020; Bhatt, 2021) suggest that, in the Beaufort  
101 Sea, the duct is persistent and widespread but not necessarily continuous; it and its acoustic  
102 effects can be non-existent, minimal, or drastic. Transmissions in the upper duct, between  
103 the surface ice and the lens, experience minimal attenuation but degrade in signal coherence  
104 with repeated reflections under the ice. In lower duct, between the lens and its conjugate  
105 depth in the Atlantic water, roughly 200 m, sound above 350 Hz is trapped near losslessly  
106 for long range propagation (Poulsen and Schmidt, 2017).

107 The Arctic, while remote, is the perfect place to demonstrate mature navigation tech-  
 108 nologies in real GNSS-denied conditions. Thorough reviews of uncrewed vehicle operations  
 109 in polar environments can be found in [Norgren et al. \(2014\)](#) and [Barker et al. \(2020\)](#); there  
 110 is no comparable work in the Arctic for a short range AUV deployment in the Beaufort  
 111 Lens. Seminal ([Bellingham et al., 1995](#); [Brooke, 1981](#); [Hayes and Morison, 2002](#); [Jackson,](#)  
 112 [1983](#); [Light and Morison, 1989](#)) and more recent AUV deployments ([Fossum et al., 2021](#);  
 113 [Jakuba et al., 2008](#); [Kukulya et al., 2010](#); [Kunz et al., 2008](#); [Plueddemann et al., 2012](#); [Tim-](#)  
 114 [mermans and Winsor, 2013](#)) witnessed the classical upward refracting sound speed profile  
 115 that is amenable to an isovelocity assumption.

116 Of note, despite different platforms and scales, are recent glider deployments in the  
 117 Canada Basin. In 2014, in partially ice-covered conditions, a long range LBL system with  
 118 WHOI Micro-Modems at 100 m exploited the lower duct for long range communication with  
 119 two gliders ([Freitag et al., 2016](#); [Webster et al., 2015](#)). The sound speed value measured at  
 120 the time of reception was used to estimate pseudorange in post-processing. The beacon-to-  
 121 beacon performance was excellent, achieving contact at ranges greater than 200 km with  
 122 a position uncertainty of 40 m. The beacon-to-glider performance, however, deteriorated  
 123 due to missed contacts outside the duct, and was not described quantitatively. In 2017,  
 124 gliders were deployed in a region with no ice coverage ([Graupe et al., 2019](#)). Ranges were  
 125 linearly scaled by a statistical description of sound speed observations taken during the  
 126 experiment,  $1450 \pm 6.5$  m/s. This resulted in an error of 550 m, which was reduced by  
 127 a factor between 4 and 5, depending on the dive, using a post-processing acoustic arrival  
 128 matching method. Both cases exploit the lower duct for high fidelity communication at

<sup>129</sup> long ranges. Unintuitively, the smaller nature of our deployment during ICEX20 is not a  
<sup>130</sup> simplifying factor. For source depths typical to vehicle operations, 30 to 200 m, a shadow  
<sup>131</sup> zone spans from 2 to 6 kilometers in range ([Schmidt and Schneider, 2016](#)).

<sup>132</sup> Compared to the previous small scale navigation efforts, the approach in this paper  
<sup>133</sup> integrates real-time model-aided data processing to estimate a representative sound speed  
<sup>134</sup> along a path from source to receiver, leveraging climatology, *in situ* data, and fast acoustic  
<sup>135</sup> modeling. The paper is organized as follows. Section [II](#) details the experimental approach  
<sup>136</sup> and conditions during ICEX20. Given that there is no GNSS ground truth for the vehicle  
<sup>137</sup> position while underway, we first evaluate the real-time ranging performance of GPS-linked  
<sup>138</sup> beacon-to-beacon communication events in section [III](#). Section [IV](#) uses insights from field  
<sup>139</sup> data to introduce a new ray filtering algorithm to improve range estimation. Section [V](#)  
<sup>140</sup> emulates the real-time processing pipeline to re-position beacon-to-beacon events and re-  
<sup>141</sup> navigate AUV *Macrura*.

<sup>142</sup> **II. OVERVIEW OF THE ICEX20 EXPERIMENT**

<sup>143</sup> The results from this paper derive from data taken while deploying the AUV *Macrura*, a  
<sup>144</sup> custom Bluefin-21, during the Ice Exercise 2020 (ICEX20), in the Beaufort Sea, from March  
<sup>145</sup> 8th to 11th. The AUV deployment was supported by the Integrated Communication and  
<sup>146</sup> Navigation Network (ICNN) ([Randeni et al., 2020, 2021; Schneider et al., 2021](#)) a special-  
<sup>147</sup> ized implementation of the LBL solution. The ICNN was initially developed via numerous  
<sup>148</sup> virtual experiments to ensure robust algorithms and interfaces between different hardware  
<sup>149</sup> components. The simulation capabilities are largely physics-driven with a modular system of  
<sup>150</sup> systems approach—an environmental simulator with sub-components for the ocean, includ-  
<sup>151</sup> ing Arctic ice drift and ocean acoustic propagation; a vehicle simulator with sub-components  
<sup>152</sup> for vehicle dynamics and navigation; a topside hardware simulator and acoustic communica-  
<sup>153</sup> tions simulator, both with a software-only configuration and a hardware-in-the-loop version  
<sup>154</sup> ([Schneider and Schmidt, 2018](#)). The virtual environment similarly emulates the interfaces  
<sup>155</sup> between the real components to test the entire software pipeline.

<sup>156</sup> **A. The Integrated Communication and Navigation Network**

<sup>157</sup> The ICNN is comprised of four ice buoys in a loose rectangle, roughly 2 km away from  
<sup>158</sup> a central ice camp with a topside computer, as shown in Fig. 1. Each ice buoy is outfitted  
<sup>159</sup> with a Garmin GPS 18x, with a pulse-per-second rising edge aligned to 1 microsecond and  
<sup>160</sup> a spec sheet accuracy of 3 m, 95% of the time. The AUV and each ice buoy are outfitted  
<sup>161</sup> with a WHOI Micro-Modem ([Singh et al., 2006](#)), with a four-element receiver array, a single

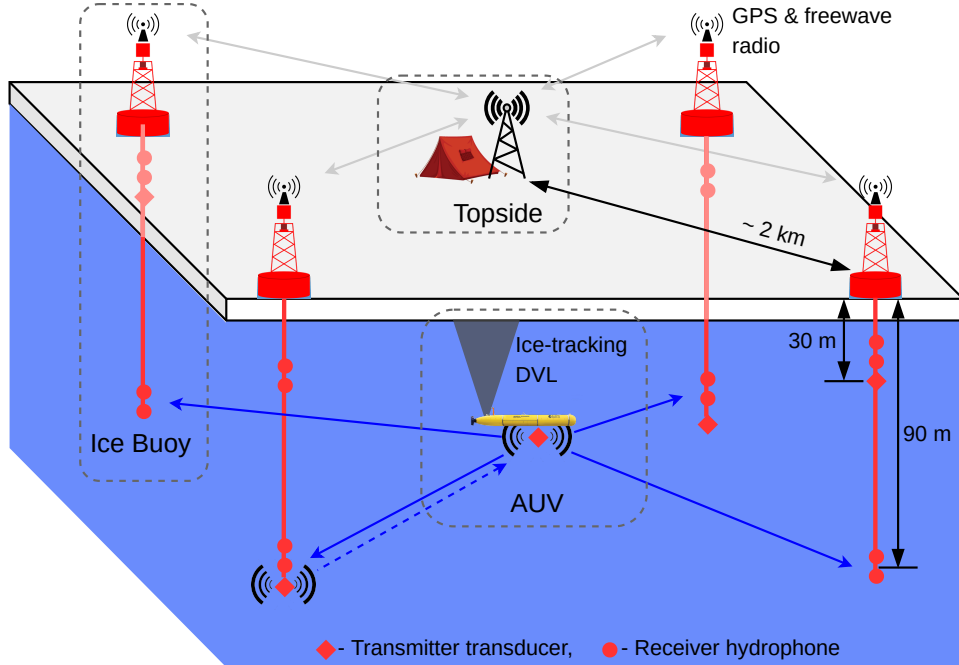


FIG. 1. A schematic overview of the Integrated Communication and Navigation Network (ICNN), which provides joint data-transfer and tracking between AUV and a human decision maker at Topside.

162 transmitter, and one-tenth of a millisecond resolution. Acoustic messages were sent with a  
 163 10 kHz carrier frequency, 5 kHz bandwidth, and phase-shift keying (PSK) modulation on  
 164 a time-division multiple access schedule with a thirty-second cycle, giving room for two-  
 165 way communication throughout the mission volume. The receive and transmit elements  
 166 were split between shallow and deeper depths—30 and 90 m—to provide better coverage  
 167 across the shadow zone. While each buoy only has one transmit depth, all buoys have both  
 168 receive depths but the active receive layer is consistent across all buoys. The design of  
 169 the ICNN enables a self-adapting network to transmit and receive at the optimal depth to  
 170 maintain contact with the AUV ([Schneider \*et al.\*, 2021](#)). The buoys do not encompass the

<sub>171</sub> full horizontal range of the vehicle but are positioned to minimize overlap in trilateration  
<sub>172</sub> for spherical positioning (Deffenbaugh *et al.*, 1996a).

<sub>173</sub> To balance competing uses of the acoustic channel, the network uses a single synchronized  
<sub>174</sub> digital communication packet to provide both tracking and data to the operator.

<sub>175</sub> 1. The AUV, running an ice-tracking DVL and an onboard hydrodynamic model, broad-  
<sub>176</sub> casts its perceived location on a scheduled, time-synchronized message via WHOI  
<sub>177</sub> Micro-Modem

<sub>178</sub> 2. Four ice buoys, each outfitted with a WHOI Micro-Modem, receive messages from the  
<sub>179</sub> AUV and send that information over freewave radio to a Topside computer

<sub>180</sub> 3. The topside computer converts travel times into pseudorange estimates using a stochas-  
<sub>181</sub> tic embedded prediction of the horizontal group velocity via BELLHOP ray tracing  
<sub>182</sub> code (Porter, 2011) using a sound speed profile provided by an updatable Virtual  
<sub>183</sub> Ocean (Bhatt *et al.*, 2022; Schneider and Schmidt, 2018)

<sub>184</sub> 4. The topside computer calculates a new position by trilaterating the range estimates  
<sub>185</sub> 5. The position differential, not the absolute position, is broadcast to the vehicle to  
<sub>186</sub> update its navigation solution and be robust to latency and intermittency

<sub>187</sub> In the face of GNSS-denied navigation, this approach was anecdotally successful, as shown  
<sub>188</sub> in Fig. 2. The AUV *Macrura* was deployed through a hydrohole from an ice camp but re-  
<sub>189</sub> covered through an emergency hydrohole. A random disk error stalled *Macrura* underneath  
<sub>190</sub> the ice but did not prevent it from transmitting its location. Due to an incoming storm, a  
<sub>191</sub> team placed a physical marker on the ice at the location. Three days later, *Macrura* was

192 found within a meter of the marker. We view the emergency recovery as qualitative proof  
 193 of the robustness of this navigation approach. Nonetheless, this paper specifically addresses  
 194 the third and fourth steps—the conversion of travel times into pseudoranges and its effect  
 195 on trilateration. By focusing on pseudorange estimates between GPS-tracked beacons, and  
 196 re-running the trilateration pipeline, the results are decoupled from all other mechanisms in  
 197 the ICNN.

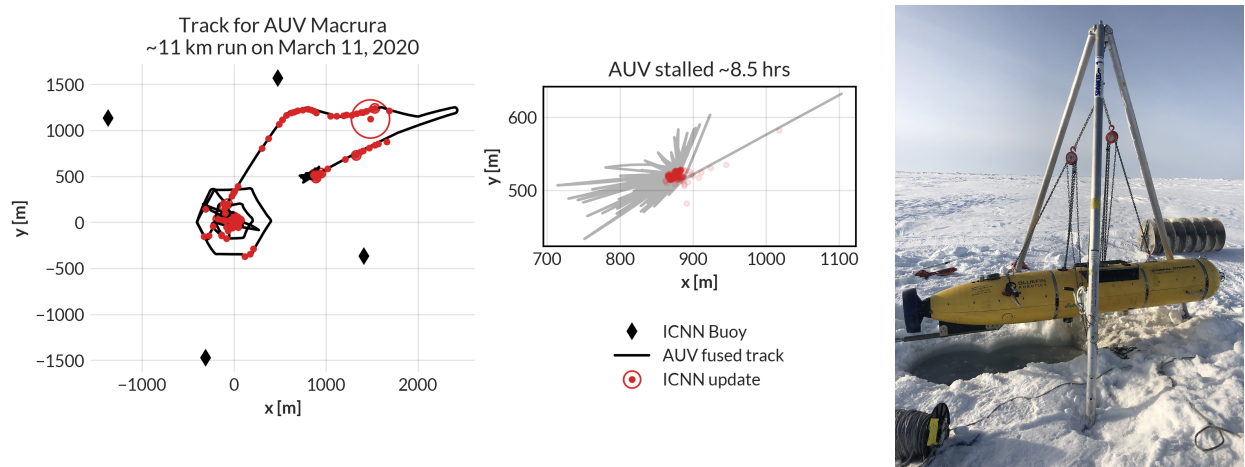


FIG. 2. The under-ice mission track for AUV *Macrura*, including the position updates as it stalled underneath the ice overnight. A marker was placed on the ice at the vehicle’s estimated self-location. It was recovered after a three day storm within a meter of the marker.

198 **B. ICEX20 sound speed conditions**

199 An important component to our navigation solution is an accurate estimation of a repre-  
 200 sentative SSP for the ocean volume. Previous field experience, during the Ice Exercise 2016  
 201 (ICEX16), demonstrated the negative effects of the Beaufort Lens on tracking and commu-

nication (Schmidt and Schneider, 2016). Fig. 3 shows historical, modeled, and *in situ* sound speed data for both ICEX16 and ICEX20. These three input streams were selected to mirror the information available on a submarine (personal conversation with LT B. Howard and LT CDR D. Goodwin). In the field, the SSP information was shared with the vehicle via basis representation compression on a lightweight digital acoustic message (Bhatt *et al.*, 2022). All modeled data comes from HYCOM (Chassignet *et al.*, 2007), which does not seem to capture the forcing mechanisms that cause the Beaufort Lens. For ICEX16, the data-driven profile was sourced from nearby Ice Tethered Profilers (ITP) after the field experiment (Krishfield *et al.*, 2008; Toole *et al.*, 2011) and exhibits a fairly low lens; the historical profile is from the World Ocean Atlas. For ICEX20, the chosen weights (data-driven) profile derives from an estimate of initial CTD casts taken on site, showing an intense warm water intrusion; the baseline (historical) profile, showing moderate ducted conditions, comes from the average of March 2013 ITP data. This month best matched sea ice and sound speed conditions at the beginning of ICEX20 (Bhatt *et al.*, 2022). It is important to note that all profiles that do show the Beaufort Lens do so with different local sound speed maxima at different depths, reflective of the wide range of lens properties observed for all ITP data in the region. The variability of the lens height and prominence is the main reason an updatable SSP was integrated into the ICNN solution.

During ICEX20, the HYCOM profile was available but never deployed. For post-processing comparison, we introduce both the HYCOM profile and an isovelocity case,  $1441.8 \pm 3.7$  m/s, as the mean and standard deviation of the observed sound speed profile over the first 200 m. This is a contrived value taken in the style of Graupe *et al.* (2019)

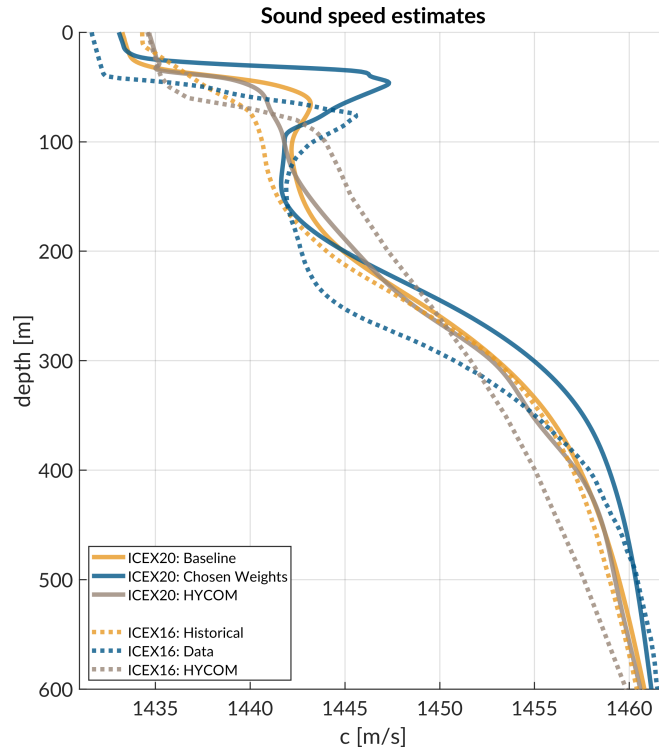


FIG. 3. Sound speed conditions for historical (baseline), data (chosen weights), and HYCOM model for both ICEX16 and ICEX20.

224 for the sake of comparison; the default value in the LAMSS simulator, which was not  
 225 environmentally informed nor used during ICEX20, was 1430 m/s.

226 **III. REAL-TIME PSEUDORANGE ANALYSIS**

227 Because the vehicle’s navigation solution during a mission can only be evaluated on the  
228 basis of the error estimates sent, a sister experiment for validating the real-time ranging  
229 approach was implemented. Ice buoy modems were run as “virtual vehicles” at a fixed  
230 depth, receiving position updates from the other beacons as well as a camp site modem  
231 lowered to 20 m. Fig. 4 shows successful events sorted by source depth. In this analysis, we  
232 assume there is insignificant displacement between the GNSS puck surface expression and  
233 subsurface modem; this is supported by unusually low observed ice drift rates, just 0.7 cm/s  
234 on average throughout the mission.

235 **A. Minimal bounce criteria (MBC)**

236 The fundamental challenge to implement GNSS-like navigation, especially in an acousti-  
237 cally complex propagation environment, is characterizing a single sound speed to compensate  
238 for the effects of ray refraction and reflection. The use of the acoustic modem network for  
239 tracking relies on the accurate estimates of travel times between the submerged platform  
240 and LBL beacons, supported by clock synchronization and a pre-determined scheduling of  
241 acoustic events. For the Beaufort Lens in particular, the strong multipath effects make it  
242 virtually impossible to deterministically predict the modem’s detected arrival time.

243 Instead, for each individual modem  $i$ , an embedded stochastic tracking framework is used  
244 to provide a running estimate of the effective sound speed  $c_{i,j}$  for the conversion from travel  
245 time to range from modem  $j$ , with the ultimate goal of matching the implied horizontal

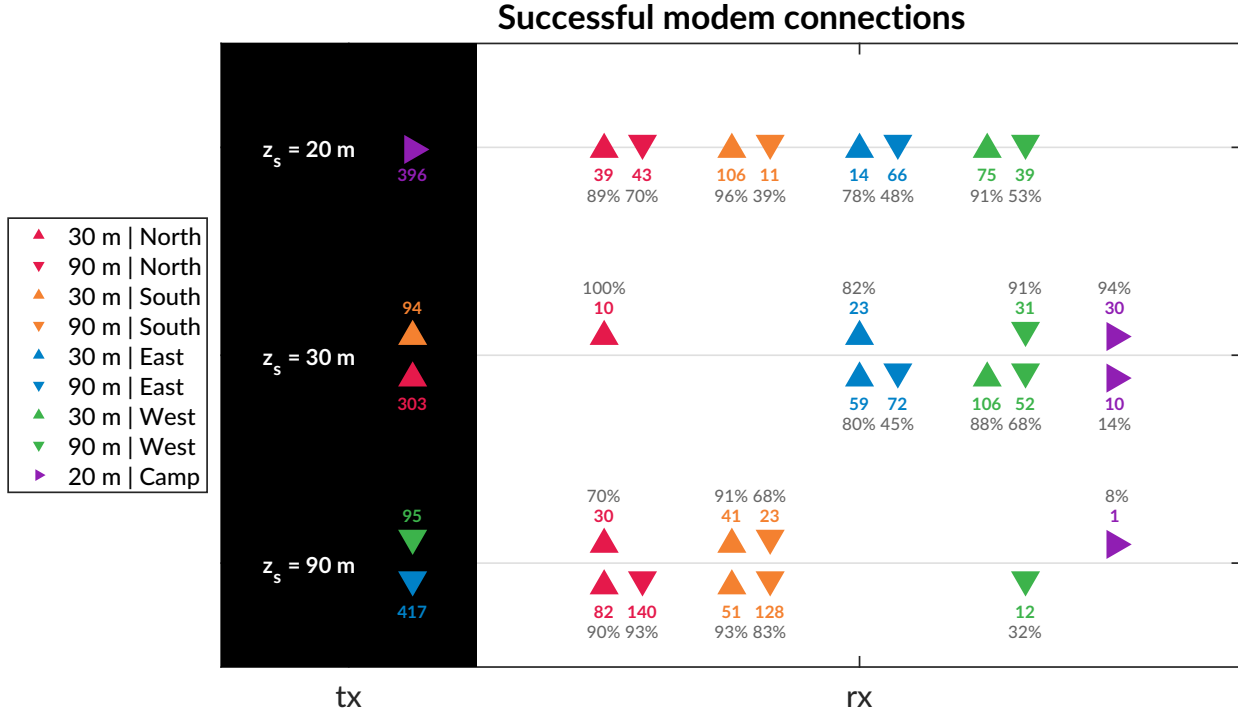


FIG. 4. An overview of the modem experiment by source and receiver depth and position. The black column on the left, *tx*, shows the source depth,  $z_s$ , with the total number of transmissions. The column on the right, *rx*, shows the receivers with the number of successful decodings and the percent success rate, defined as the ratio of decoded to detected. The orientation of the triangles—sideways, upwards, and downwards—corresponds to depths of 20, 30, and 90 m.

<sup>246</sup> effective sound speed, i.e., the GPS-recorded distance between two nodes divided by the  
<sup>247</sup> modem-recorded one way travel time between them.

<sup>248</sup> In the ICEX20 configuration, the acoustic tracking is running on the topside computer,  
<sup>249</sup> which controls the ICNN. Here we assume that the effective sound speeds  $c_{i,j}$  are smoothly

250 varying over the course of a vehicle mission, i.e., with respect to range, mission time, and  
 251 the thirty-second frequency.

252 When the topside tracking framework receives a message, with a time delay,  $\Delta t$ , it will  
 253 request a new estimate for  $c_{i,j}$  along with its standard deviation. The effective sound speed  
 254 is predicted using the vehicle's reported depth and the extrapolated navigation solution for  
 255 range,  $\hat{r}$ , as inputs to the ray tracing program, which returns an impulse response estimate  
 256 in the form of ray travel times  $dt_j$  and amplitudes  $a_j$ .

257 The initial call to BELLHOP is over a local grid centered at the range and depth posited  
 258 by the onboard tracking solution. The grid, compared to a point solver, adds redundancy  
 259 in resolving the actual multipath structure for a reliable acoustic path without overtaxing  
 260 onboard computational time and memory. It is initialized as  $11 \times 11$  points spanning 10  
 261 m horizontally and 20 m vertically. The horizontal dimension reflects the accumulated  
 262 vehicle position error given a thirty-second communication cycle; the vertical dimension  
 263 reflects how, computationally, eigenrays of the same timefront seem to stack vertically in  
 264 the water column. For each grid point, BELLHOP produces a number of arrivals resulting  
 265 from multiple propagation paths. Using only the  $N_0$  rays with neither surface nor bottom  
 266 bounces, it will then estimate the current effective sound speed  $c$  from a power weighted  
 267 average of the ray travel times,

$$c = \frac{\hat{r} \sum_{n=1}^{N_0} a_n^2}{\sum_{n=1}^{N_0} dt_n a_n^2}, \quad (1)$$

268 and the associated weighted standard deviation,

$$\sigma_c \simeq \sqrt{\frac{\sum_{n=1}^{N_0} (dt_n - \hat{r}/u)^2 a_n^2}{\sum_{n=1}^{N_0} a_n^2}} \frac{u^2}{\hat{r}} \quad (2)$$

<sup>269</sup> If no direct paths exist, i.e.  $N_0 = 0$ , then the effective speed is computed using the same  
<sup>270</sup> algorithm for the ray arrivals with one bounce, and so on.

<sup>271</sup> Finally, the pseudorange is calculated simply as

$$r_{i,j} = c_{i,j} \Delta t_{i,j} \quad (3)$$

<sup>272</sup> Thus the MBC method assumes the signal detected by the modem will be dominated by  
<sup>273</sup> a set of paths with the least number of boundary interactions. Importantly, this stochastic,  
<sup>274</sup> ensemble method for group velocity calculation can run in real-time, appearing to be orders  
<sup>275</sup> of magnitude faster than other post-processing methods which seek to determine the specific  
<sup>276</sup> ray itself that best matches a prominent indicator from the arrival structure. The BELLHOP  
<sup>277</sup> simulation that runs this calculation uses 3600 rays with launch angle fan of -60 to 60 degrees,  
<sup>278</sup> a representative depth dependent sound speed profile, and a range dependent bathymetry.

## <sup>279</sup> B. Pseudorange error metrics

<sup>280</sup> The sister modem experiment generated 811 beacon to beacon communication events with  
<sup>281</sup> their own real-time MBC group velocity predictions. Given the complexity of the ICNN  
<sup>282</sup> system, this experiment did not collect an exhaustive set of data across all buoy, source  
<sup>283</sup> depth, receive depth, and sound speed combinations. The algorithm generally overestimates  
<sup>284</sup> pseudoranges because it resolves the effective sound speed for the most direct path.

<sup>285</sup> Fig. 5 shows the range error boundary for both SSP inputs used in ICEX20. A promising  
<sup>286</sup> sign that the MBC method adapts sound speed somewhat intelligently is the lack of error  
<sup>287</sup> growth as travel time increases. The baseline SSP ( $n=243$  events) has an absolute pseudor-

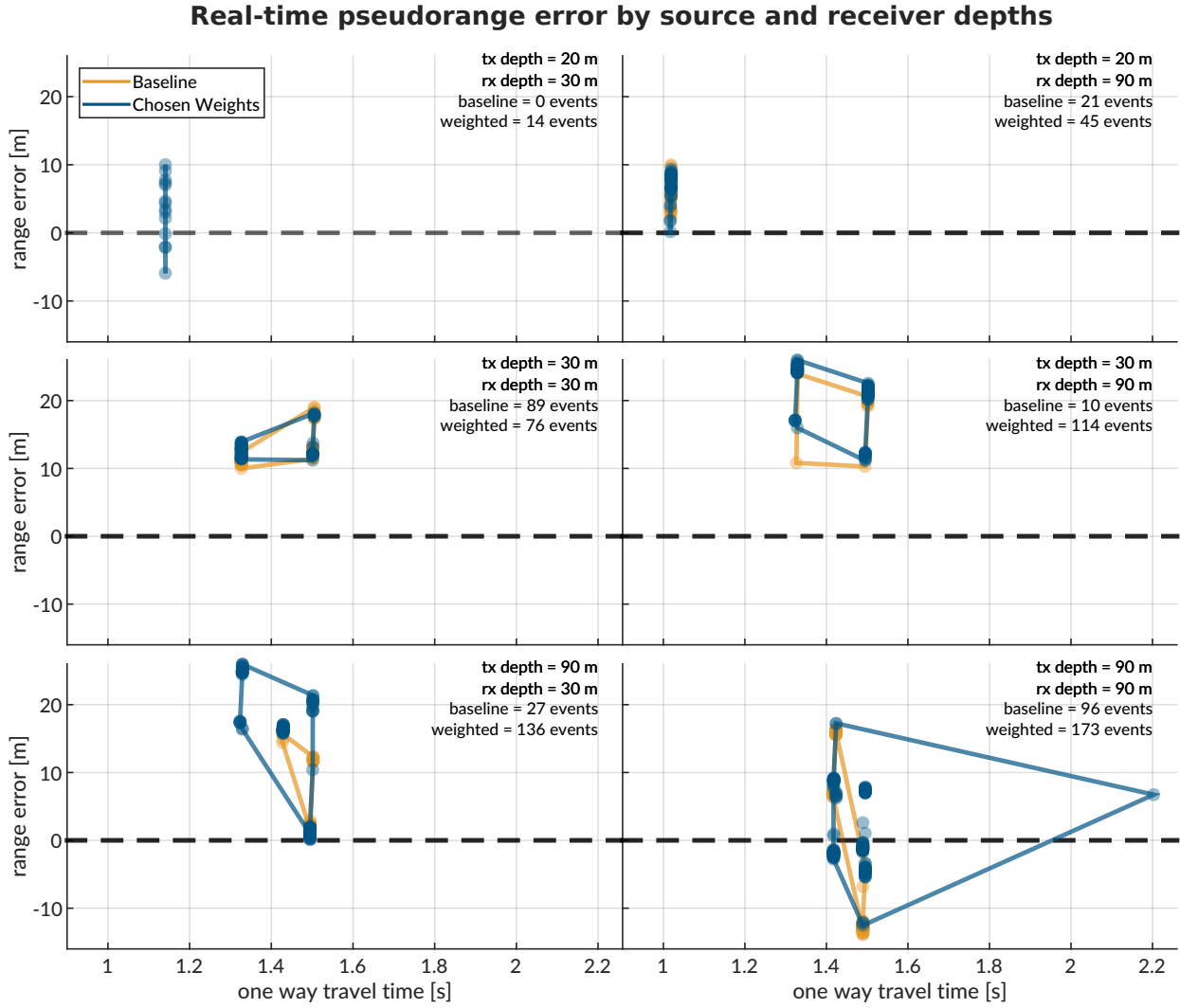


FIG. 5. The real-time range error by source (rows: 20, 30, and 90 m) and receiver (columns: 30 and 90 m) pairings for both sound speed estimates used during ICEX20. The amount of communication events is notated in the top right of each panel. The dashed line indicates no range error, and the boundary drawn indicates scope of the range error as a function of one way travel time.

288 range error of  $11.38 \pm 4.23$  m; the weighted SSP ( $n=568$ ),  $11.36 \pm 8.12$  m. The discrepancy  
 289 between these two is largely due to outlier events only contained in the weighted SSP set.  
 290 Where there is overlap between sound speed conditions used for the real-time MBC, the

291 pseudorange error difference is no more than a few meters. The overarching results show  
 292 that sound speed estimates derived from eigenrays for a local grid, as opposed to a singular  
 293 point, are accurate enough to support vehicle navigation. While the NBC looks for just the  
 294 least complex multipath, the high density of launch angles almost always guarantees a direct  
 295 path. Nonetheless, the consistent overestimation of pseudorange invites further analysis into  
 296 acoustic arrival matching.

### 297 C. Eigenray identification for beacon-to-beacon events

298

299 Accounting for ice movement between beacons creates nominal ranges with small vari-  
 300 ability. Figs. 6, 7, and 8 show eigenrays for three sound speed environments for source  
 301 depths of 20, 30, and 90 m, respectively. Eigenrays were initially found using the built-in  
 302 BELLHOP protocol with a launch angle fan of 2400 rays between -60 and 60 degrees. Sepa-  
 303 rately, recorded travel times between beacons were clustered with 1 millisecond boundaries  
 304 such that some source-receiver pairs had multiple, distinct travel times to approximate. The  
 305 BELLHOP eigenray returns were then filtered such that one was selected per travel time  
 306 cluster, in the hopes that the eigenray will converge to the receiver locations for the most  
 307 realistic sound speed input. It should be noted that bottom bounces were recovered but  
 308 filtered out. The three source depths create distinct ray geometries with respect to the three  
 309 sound speed inputs.

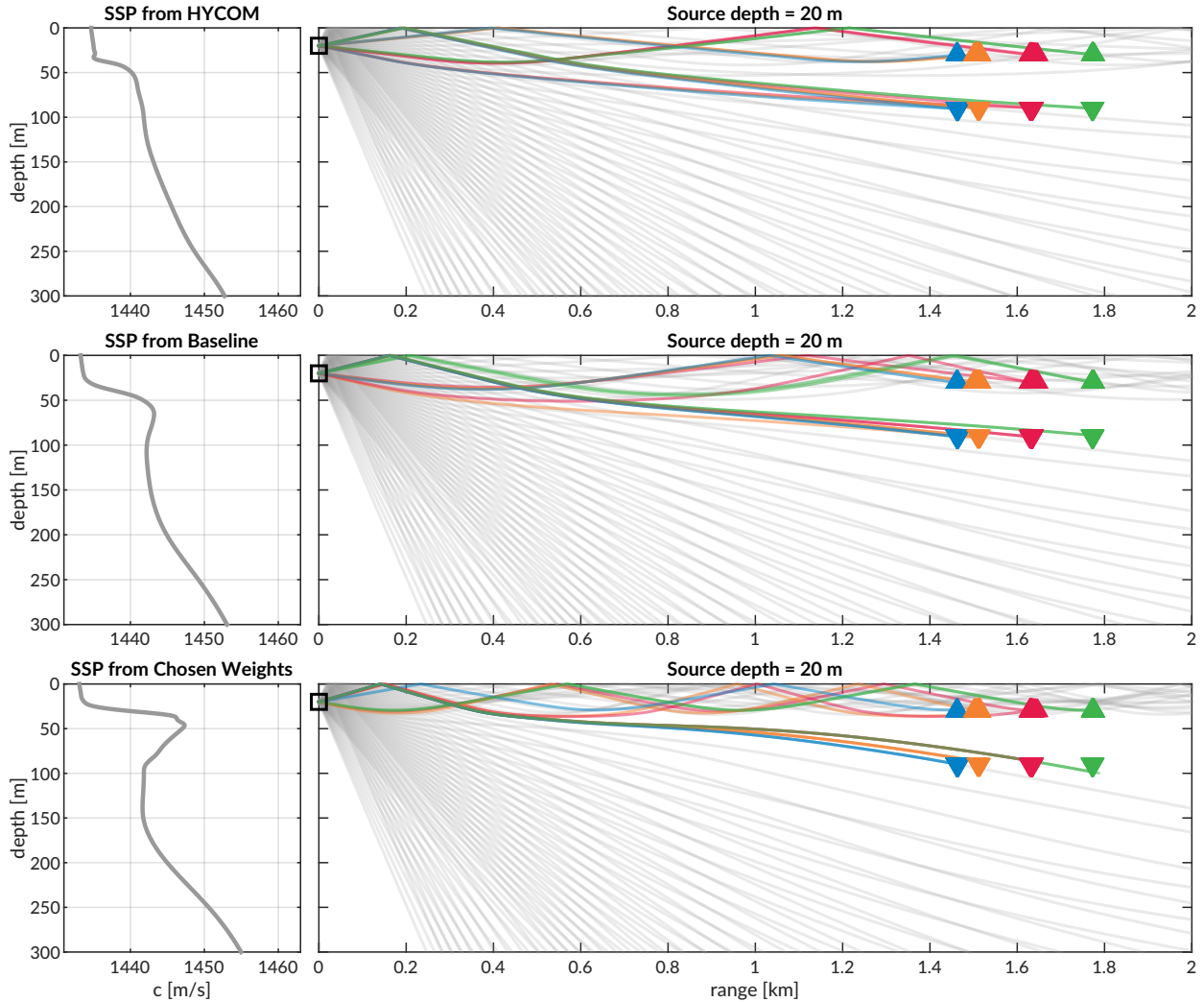
310 **1. Source depth of 20 m**

FIG. 6. Eigenrays for beacon-to-beacon events for each sound speed with a nominal source depth of 20 m over a total ray fan in gray. The beacons are highlighted in color/marker coding in Fig. 4.

311 For a source at 20 m in depth, shown in Fig. 6, reliable eigenrays are found for all sound  
 312 speed inputs. Rays refract upwards and neatly intersect with the shallow and deep receiver  
 313 locations between 1.5 and 1.8 km in range. However, the ray paths for the shallow receivers  
 314 change both in the number of surface interactions and where the surface interactions occur

315 with respect to range across the SSPs. As the Beaufort Lens strengthens, the chosen paths to  
 316 the second farthest shallow buoy (North, in red) interact with the surface more and become  
 317 distinct. The weighted SSP shows the most interesting effects for the deeper receivers. The  
 318 ray paths all interact with the surface and the eigenrays for the Northern (red) and Western  
 319 (green) buoys are in fact the same ray.

320        ***2. Source depth of 30 m***

321        The ray geometries from the 30 m source, shown in Fig. 6, show a similar degradation  
 322 of eigenray identification with increased ducting. Receptions span 1.5 to 3.2 km. Once  
 323 again, eigenrays for HYCOM and the baseline SSP are visually appropriate. Rays for the  
 324 weighted SSP show how the surface channel intensifies ice interactions and how the shadow  
 325 zone denies reliable acoustic paths. Pointedly, the increasing number of surface reflections to  
 326 the farthest shallow buoy (North, in red) crystallize the MBC's tendency for overestimation.  
 327 For the HYCOM, baseline, and weighted SSP inputs, the most appropriate eigenrays show  
 328 2, 3, and 4 surface interactions.

329        ***3. Source depth of 90 m***

330        Lastly, Fig. 8 shows ray geometries from the 90 m source, elucidating a different extent  
 331 of the shadow zone. While the receiver locations are similar to that of the 30 m source  
 332 depth, the deeper source depth effectively negates the upper duct and places the upper (and  
 333 some of the lower) receivers in unreliable acoustic paths. The HYCOM eigenrays still show  
 334 the most reliable acoustic paths that deteriorate with increasing ducted conditions. The

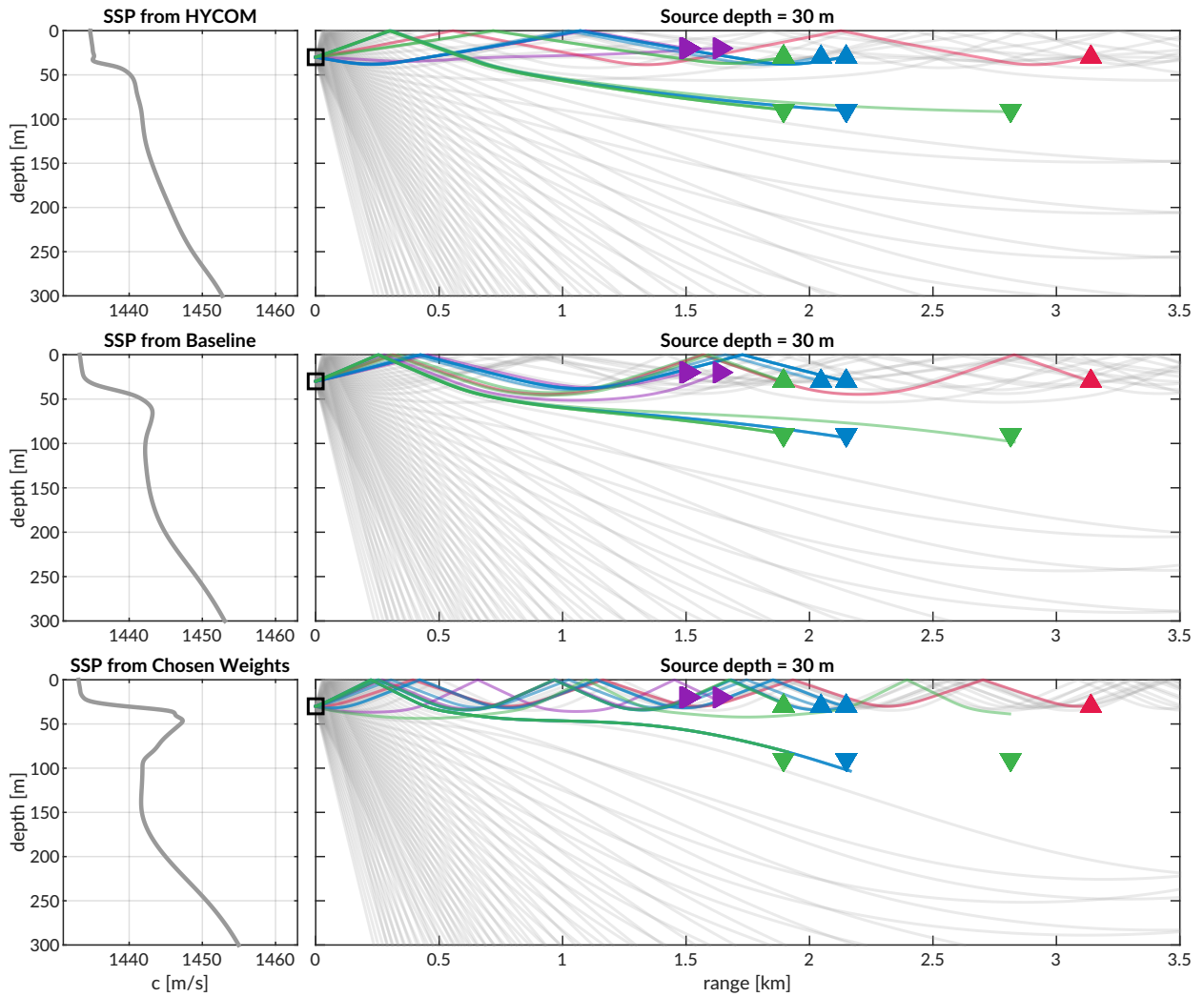


FIG. 7. Eigenrays for beacon-to-beacon events for each sound speed with a nominal source depth of 30 m over a total ray fan in gray. The beacons are highlighted in color/marker coding in Fig. 4.

<sup>335</sup> lack of direct paths from the observed SSP further points out the shortcomings of the MBC

<sup>336</sup> approach.

<sup>337</sup> The goal of the MBC algorithm was to provide a reliable, physically intuitive interpretation  
<sup>338</sup> of the acoustic propagation without taking on the additional burden of regularly identifying specific paths that may connect any given source-receiver pair in the network.

<sup>340</sup> While it was unlikely to resolve multipath arrivals that triggered successful modem detec-

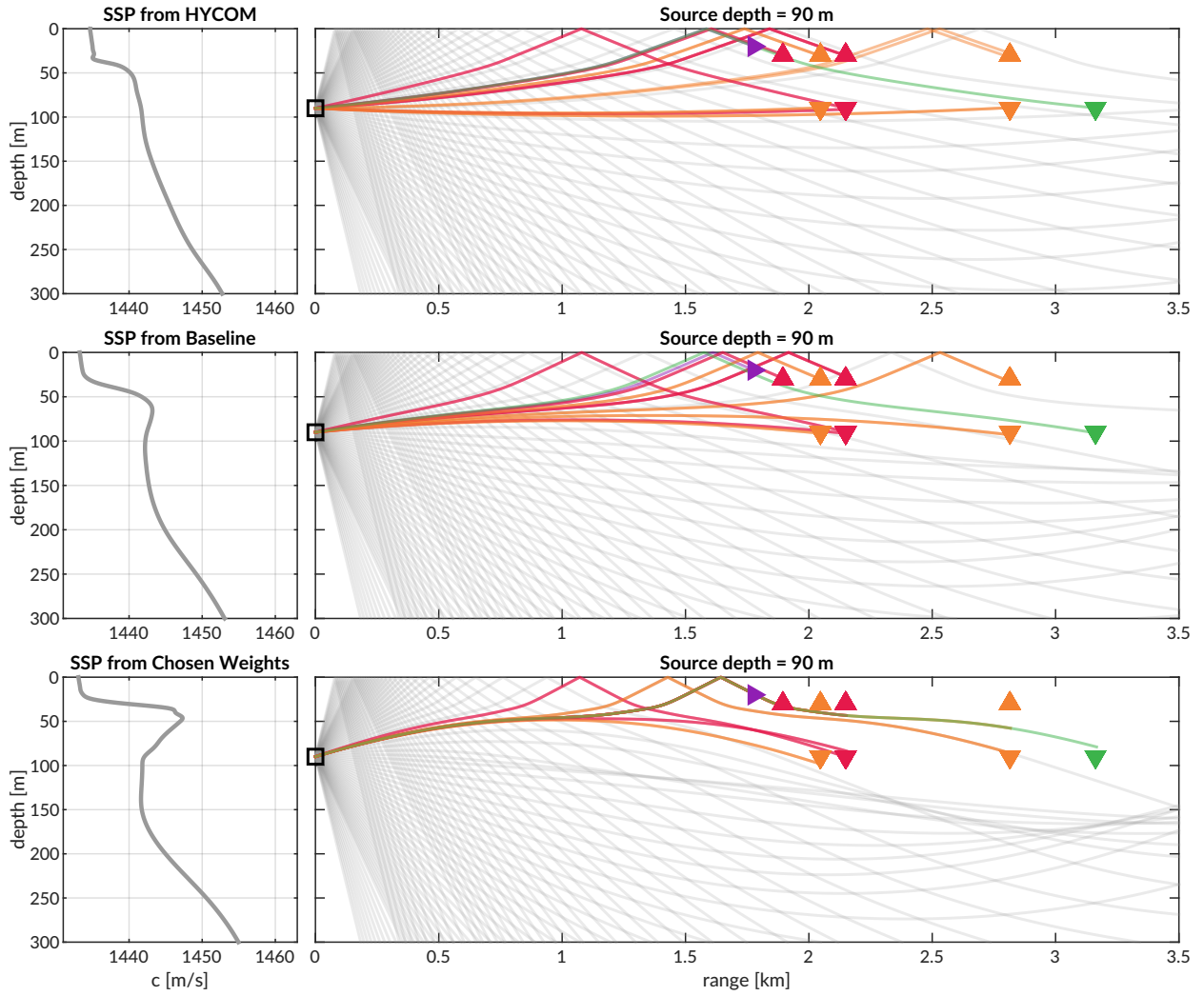


FIG. 8. Eigenrays for beacon-to-beacon events for each sound speed with a nominal source depth of 90 m over a total ray fan in gray. The beacons are highlighted in color/marker coding in Fig. 4.

<sup>341</sup> tion, an isovelocity approach would have provided no adaptivity against source and receiver  
<sup>342</sup> depth differences. Its performance was adequate for vehicle navigation and would have likely  
<sup>343</sup> sufficed if it were not for the prominence of the duct observed relative that of other model  
<sup>344</sup> and data products.

<sup>345</sup> **IV. POST-PROCESSED PSEUDORANGE ANALYSIS**

<sup>346</sup> From all events recorded during the modem test experiment, there are 1242 successfully  
<sup>347</sup> decoded beacon-to-beacon events. Thus, a post-processing analysis that emulates the real-  
<sup>348</sup> time navigation engine was run to overcome the unequal distribution of communication  
<sup>349</sup> events with respect to depth, range, and sound speed status.

<sup>350</sup> It is important to note that the value for the extrapolated range,  $\hat{r}$ , is only tracked when  
<sup>351</sup> the modem runs the vehicle behavior; thus we replace  $\hat{r}$  with the GPS-tracked range for  
<sup>352</sup> all modem events. Because  $\hat{r}$  converges to the correct solution, a comparison of  $\hat{r}$  with the  
<sup>353</sup> GPS-tracked range shows a normal, zero-centered distribution within the bounds of GPS  
<sup>354</sup> drift. The analysis therefore seeds realistic but “omniscient” knowledge of the extrapolated  
<sup>355</sup> range and emulates the post-processing pipeline to more thoroughly evaluate the acoustic  
<sup>356</sup> pseudorange estimate for all modem events. Sound speed inputs are the isovelocity sound  
<sup>357</sup> speed in addition to the modeled, baseline, and weighted SSPs from Fig. 3. The analysis  
<sup>358</sup> replicates the MBC but also introduces a new filtering algorithm, the nearest bounce criteria  
<sup>359</sup> (NBC), based on insights gleaned from the eigenray analysis. Accordingly, the results in  
<sup>360</sup> this section evaluate the utility of the algorithms and sound speed sources, divorced from  
<sup>361</sup> their role in the ICNN while maintaining real-time relevance.

<sup>362</sup> **A. Nearest bounce criteria (NBC)**

<sup>363</sup> The extent of ray bending and repeated reflections is extremely dependent on the degree  
<sup>364</sup> of the Beaufort Lens observed. Based on this insight, a new algorithm, the nearest bounce

<sup>365</sup> criteria (NBC), is a slight modification from the MBC and includes multipath as a new  
<sup>366</sup> dimension of information to exploit. This metric, while run in post-processing, adds a  
<sup>367</sup> negligible amount of computation for real-time efficacy.

<sup>368</sup> Given a running estimate for the effective sound speed  $c_{i,j}$  between nodes  $i$  and  $j$ , the  
<sup>369</sup> navigation system has an extrapolated value for range,  $\hat{r}$ , and a recorded travel time,  $\Delta t_{i,j}$ .  
<sup>370</sup> Instead of using only the  $N_0$  rays with neither surface nor bottom bounces to estimate  
<sup>371</sup> conversion speed, and subsequently moving to incremental number of bounces only when no  
<sup>372</sup> valid direct path solutions exist, we solve for the power weighted average of the ray travel  
<sup>373</sup> time for the  $N_k$  rays with  $k$  bounces,

$$t_k = \frac{\sum_{n=1}^{N_k} dt_n a_n^2}{\sum_{n=1}^{N_k} a_n^2}, \quad (4)$$

<sup>374</sup> find the nearest matching power weighted average to recorded travel time,

$$t_{i,j,k} = \min_{k=0,1,2,\dots} |t_k - \Delta t_{i,j}| \quad (5)$$

<sup>375</sup> predict an effective sound speed,

$$c_{i,j} = \frac{\hat{r}}{t_{i,j,k}} \quad (6)$$

<sup>376</sup> and estimate the range as was done previously.

$$r_{i,j} = c_{i,j} \Delta t_{i,j} \quad (7)$$

<sup>377</sup> Whereas the MBC outputs a scalar, this method first outputs a vector of effective sound  
<sup>378</sup> speeds based on the number of reflections. Then a single value is selected that best matches  
<sup>379</sup> the recorded travel time, as the detected arrival is not always the first arrival or the direct  
<sup>380</sup> path and could even be masked by noise or blocked temporarily ([Deffenbaugh \*et al.\*, 1996b](#)).

<sup>381</sup> We manually cap the number of bounces at four because of the smaller operational scale and  
<sup>382</sup> the attenuation accrued with many surface interactions. Bottom bounces are not encoded  
<sup>383</sup> separately because of ray's tendency to refract upward, not due to information limitations.

<sup>384</sup> **B. Effective sound speed predictions**

<sup>385</sup> The minimal and nearest bounce algorithms are applied with the three sound speed inputs  
<sup>386</sup> shown in Figs. 6, 7, 8. The resulting predicted effective sound speeds are shown in Fig. 9  
<sup>387</sup> for all source depths versus one way travel time.

<sup>388</sup> The goal of the effective sound speed prediction is to converge towards the implied sound  
<sup>389</sup> speed, i.e. the GNSS-derived range divided by the recorded travel time. As the environ-  
<sup>390</sup> mental and ray filtering method become better representations of the real ocean, the lower  
<sup>391</sup> the expected mismatch is between the implied and estimated effective sound speeds.

<sup>392</sup> The various sound speed inputs—isovelocity aside—not only modify the predicted effec-  
<sup>393</sup> tive sound speed, as seen by the colored vertical offsets, but often classify a distinct number  
<sup>394</sup> of bounces. HYCOM sees the most direct and one bounce multipath structures, lending a  
<sup>395</sup> bias for faster speeds; the weighted SSP sees the most double and triple bounces, favoring  
<sup>396</sup> slower speeds; the baseline sound speed exists in between. Very rarely is the multipath  
<sup>397</sup> structure classified as a direct path, where the MBC and NBC would prediction overlap. In  
<sup>398</sup> fact, the higher the multipath classification, the more accurate the sound speed prediction

<sup>399</sup> is, likely driven by a tighter or even sparser bundle of rays. Discontinuities in multipath  
<sup>400</sup> classification provide initial evidence for its importance to a smoothly varying group velocity,  
<sup>401</sup> as shown in the cluster of 30 to 30 m transmissions in 9, where HYCOM jumps from one to

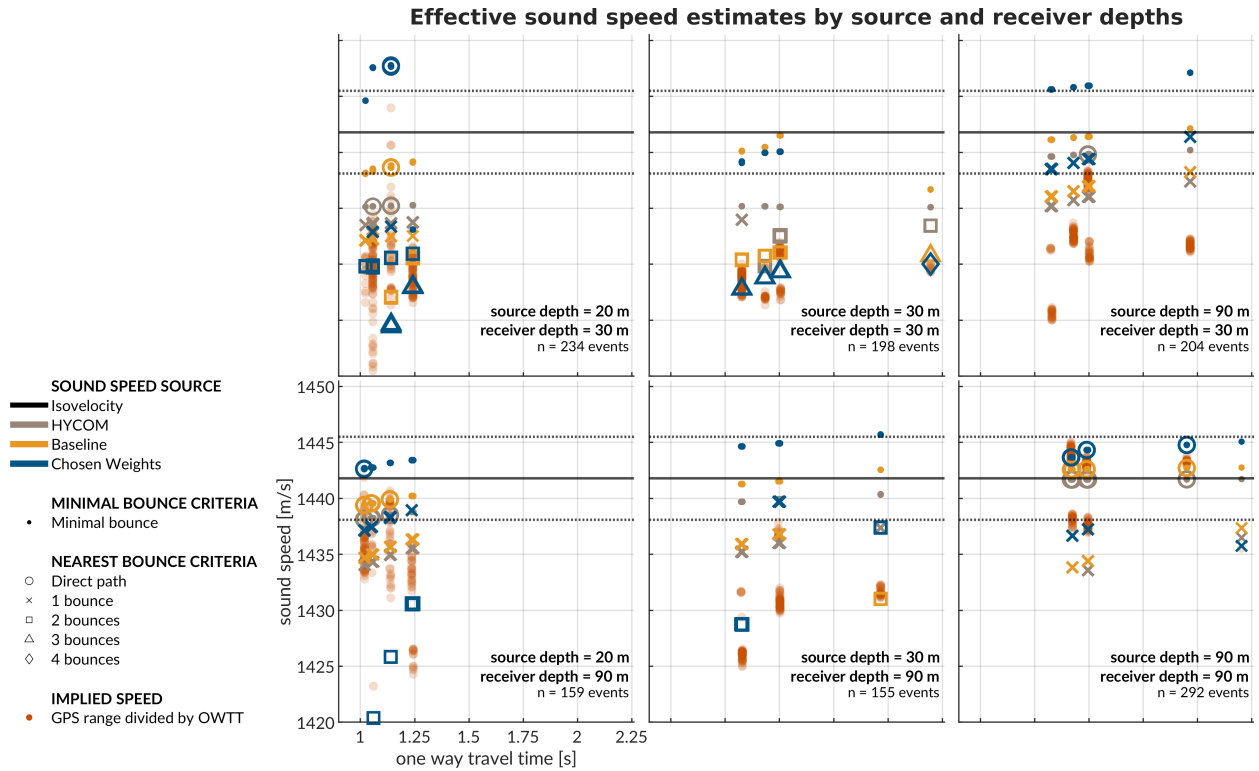


FIG. 9. A post-processing comparison of effective sound speed predictions for all beacon-to-beacon events. The rows share receiver depth; the columns share source depth. The recorded travel time is on the x-axis and the predicted effective sound speed is on the y-axis. The sound speed source is indicated by color. The isovelocity is shown as the mean  $\pm$  the standard deviation. The minimal and nearest bounce criterion are distinguished by different marker shapes, compared to the separately colored red dots showing the implied calculation.

402 two classified bounces amidst the baseline SSP and weighted SSP smoothly increasing while  
 403 consistently seeing two and three classified bounces, respectively. Of course, the prediction  
 404 deteriorates with cross-layer transmissions across the duct, but not to the same degree at  
 405 which eigenrays could not be found for the weighted SSP in section III C. The evidence sug-

<sup>406</sup> gests that the grid based method provides a useful amount of redundancy to resolve similar  
<sup>407</sup> enough eigenrays.

<sup>408</sup> It is useful to think about in what case the isovelocity—or any isovelocity framing—would  
<sup>409</sup> have been appropriate. The transmissions from shallow to shallow receiver would may have  
<sup>410</sup> matched the default configuration of 1430 m/s. The isovelocity contrived for this paper,  
<sup>411</sup> 1441.8 m/s, best matches the transmissions from 90 to 90 m. The one from [Graupe \*et al.\*](#)  
<sup>412</sup> ([2019](#)), 1450 m/s, would have had a systemic overestimation. In addition, over the course  
<sup>413</sup> of the four day experiment, the local maxima of the Beaufort Lens changed from roughly  
<sup>414</sup> 1447 m/s at 40 m to 1442 m/s at 60 m. Given that implied sound speeds just for beacon-  
<sup>415</sup> to-beacon events span 1420 to 1445 m/s, it is safe to say that a nominal sound speed would  
<sup>416</sup> sacrifice pseudorange accuracy somewhere, and that an adaptive approach is necessary even  
<sup>417</sup> for short and/or small scale operations in the Beaufort Lens.

### <sup>418</sup> C. Pseudorange error metrics

<sup>419</sup> Pseudorange estimation plays an important role in trilateration. Fig. [10](#) shows the  
<sup>420</sup> directional pseudorange error “footprints” for the four sound speed inputs with the NBC  
<sup>421</sup> approach, separated by source and receiver depth configurations.

<sup>422</sup> The weighted SSP range error generally has the smallest and most zero-centered footprint.  
<sup>423</sup> The one case it does not is for the source-receiver pairings between 30 and 90 m in depth. The  
<sup>424</sup> increased error for these is most likely driven by the computational artifacts encountered  
<sup>425</sup> when propagating through the steep sound speed gradients of the lens and through the

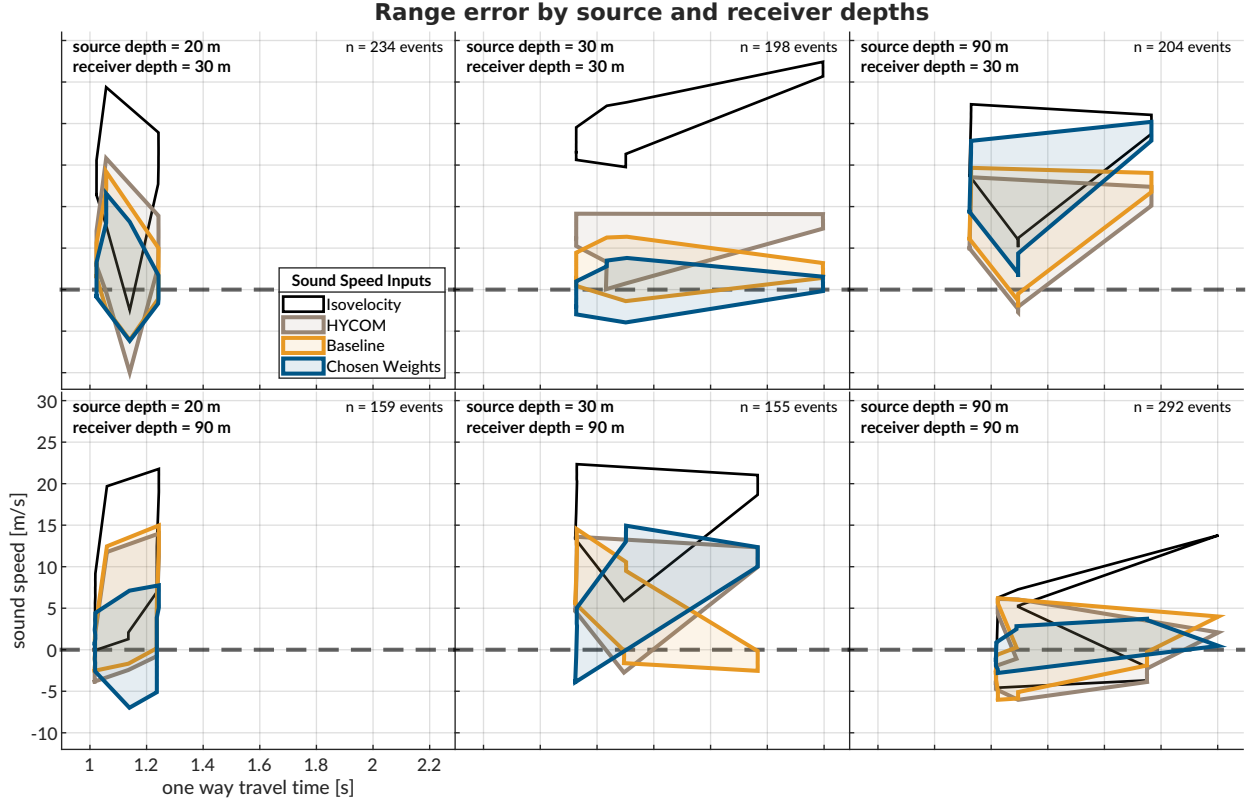


FIG. 10. The post-processed pseudorange error; the rows share receiver depth; the columns share source depth. The dashed gray line shows no error. The shaded region connects the range performance across all events.

<sup>426</sup> shadow zone. All other source depth pairings are significantly improved using the chosen  
<sup>427</sup> weights compared to HYCOM or the baseline.

<sup>428</sup> When using a linear scaling to convert travel time into range, any offset between the  
<sup>429</sup> assumed sound speed and the horizontal group velocity produces unconstrained error with  
<sup>430</sup> increasing receiver distance, whereas an adaptive estimate would exhibit no such trend. This  
<sup>431</sup> is easily observed in the same-layer links, i.e., 30 to 30 m and 90 to 90 m. In cross-layer  
<sup>432</sup> links, the isovelocity does not perform better but tends to exaggerate or flip the footprint  
<sup>433</sup> created adaptively.

434 The improvement from MBC to NBC is most evident for the data-driven sound speed;  
435 while the HYCOM SSP improves from a median absolute range error of 6.41 to 4.61 m,  
436 the baseline SSP improves from 10.30 to 2.27 m, and the weighted SSP improves from  
437 13.28 to 2.12 m. In comparison, the isovelocity has a median error of 13.09 m. The order  
438 of magnitude improvement in the ducted SSPs demonstrate the effectiveness of the NBC  
439 algorithm exploiting the observed multipath conditions.

440 There is one example that helpfully illustrates the improvement brought upon by bounce  
441 classification. For transmissions between North and South at 30 m, the OWTT spread is  
442 2.1958 to 2.1963 s; the GNSS-tracked distance is 3138.54 to 3140.87 m; and the implied  
443 effective sound speed is 1429.3 to 1430.1 m/s. For these transmissions, the weighted SSP  
444 and the MBC approach produce a pseudorange error of -1491 m, as the effective sound speed  
445 is dominated by bottom bounce arrivals with much greater travel times. The NBC approach  
446 categorizes this same record as a quadruple surface bounce, reducing the pseudorange error  
447 to less than a meter. Comparatively, the NBC approach for HYCOM and the baseline  
448 SSP produce pseudorange errors of 8.30 and 2.39 m, respectively. There is strong evidence  
449 to suggest that the sound speed and multipath fidelity codependently improve localization  
450 accuracy.

**451 V. TRILATERATION FOR ICEX20 FIELD DATA**

452 To overcome potentially intermittent acoustic communication, the operational paradigm  
 453 of the ICNN computes corrections relative to the trilaterated position estimates transmitted  
 454 by the vehicle, rather than transmitting the updated positions themselves. The reliability of  
 455 the correction is directly linked to how accurately the travel time measurements are converted  
 456 to pseudoranges. This section aims to resolve that tension by reevaluating the trilateration  
 457 results with respect to the MBC and NBC algorithms. The MBC/NBC effective speed  
 458 predictions were tracked independently for each source-receiver pair; although the sound  
 459 speed was expected to be locally smooth near a given receiver, no such assumption was  
 460 enforced between distinct acoustic links.

**461 A. Re-positioning beacon to beacon events**

462 When the beacons ran as virtual vehicles, the ICNN did not have access to that buoy's  
 463 GPS data stream except for what was sent via digital acoustic message. The static nature of  
 464 the experiment means that the initial estimate transmitted to the ICNN was in fact a ground  
 465 truth position. Therefore, a distribution of corrections from the ICNN, as shown in Fig. 11,  
 466 reflects positioning accuracy. The NBC clearly outperforms the MBC, with almost 80% of  
 467 the corrections below 6 meters and the median within the deployed GNSS puck precision  
 468 of 3 meters. By contrast, the MBC shows roughly 20% within the GNSS puck precision,  
 469 and separate peaks from 9–12 meters and 21–27 meters. This trimodal nature reflects the  
 470 distribution of reflections on the ice surface.

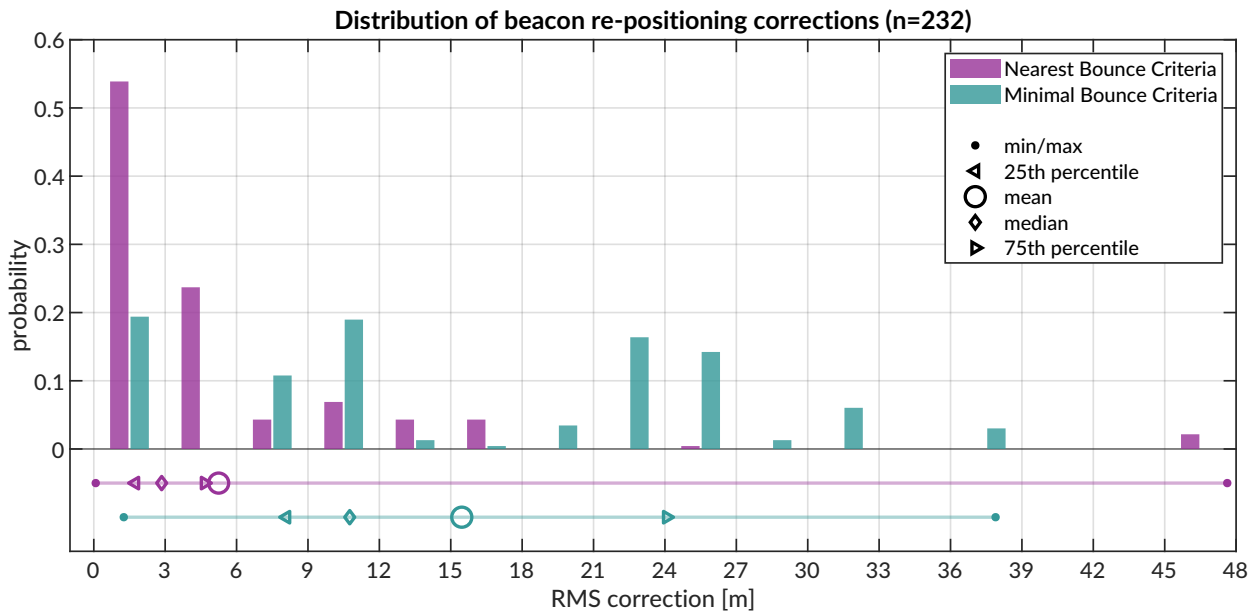


FIG. 11. Trilateration events; however, 264 entries are 2-beacon solutions, 22 are 3-beacon, and 2 are 4-beacon. When limited to only two ranging circles, the trilateration chooses the closer of the two intersection points. The x-axis is cut off at the upper limit for the NBC algorithm.

471 In several events, the MBC is unable to accurately estimate the effective sound speed for  
 472 one of the acoustic links, leading to a large positioning error. The NBC, however, better  
 473 resolves an approximation of the acoustic path. For example, in some trilateration solutions  
 474 for the Eastern buoy, the MBC shows a correction of more than a kilometer; the NBC is  
 475 two orders of magnitudes less.

476 **B. Re-navigating AUV *Macrura***

477 Up to this point, pseudorange estimation and localization have been evaluated on GPS-  
 478 linked beacon-to-beacon connections to validate the NBC algorithm. This analysis ports the  
 479 MBC and NBC algorithms to re-navigate the AUV *Macrura*.

480 In comparison to the modem experiment, the AUV data clearly exhibit instances where  
481 a receiver detects the same transmission more than once. This is not surprising considering  
482 the complex multipath provided by the Beaufort Lens. The 11 hour vehicle mission con-  
483 tains 3,260 transmissions, 12,938 total detections, and 4,704 successful receptions. Allowing  
484 receptions with PSK errors would almost double the number of recorded multipath arrivals  
485 exploited for positioning, if a real-time solution could correctly parse paths from different  
486 arrivals in the same thirty-second cycle. Thus it remains a future endeavor to explore how  
487 failure mode information from acoustic modems could be used to identify unsuccessful but  
488 otherwise trustworthy arrivals to augment trilateration samples.

489 The following performance analysis is constrained to what the vehicle acted on in real-  
490 time. AUV *Macrura* and the ICNN ran an adaptive depth behavior to maintain acoustic  
491 communication on the insight that cross-layer links were more likely to fail than same-layer  
492 ones. Accordingly, the vehicle dove deeper than 50 meters about 20% of the time it was  
493 underway.

494 In contrast to the modem tests, where position correction illustrated re-positioning ac-  
495 curacy, the re-navigation corrections are less valuable in the absence of GNSS ground truth.  
496 The correction magnitude necessarily depends on the vehicle's internal navigation estimate,  
497 which is prone to larger errors from sensor drifts, ocean currents, and other error not cap-  
498 tured in the hydrodynamic model. Thus, larger corrections are not necessarily indicative of  
499 worse performance. Navigation accuracy is better described by trilateration error, the RMS  
500 of the remaining pseudorange errors from each acoustic link.

501 Fig. 12 shows the correction magnitudes and trilateration errors for events with three or  
 502 more receptions during AUV operations. Whereas the MBC has a fairly bimodal nature,  
 503 with peaks centered around 10–15 and 35–40 m, the NBC favors smaller corrections, from  
 504 5–20 m, and has a long tail. The distribution of corrections are much larger than the  
 505 distribution of RMS error. It is apparent that, while both methods are quite successful,  
 506 there is strong evidence that the NBC achieves single meter accuracy.

### 507 C. Investigating potential GNSS noise

508

509 The fact that the bulk of the best performing re-navigation error exists within the pre-  
 510 cision of the GNSS unit deployed invites a further look into GNSS noise. In the Arctic,  
 511 GNSS performance worsens due to poor constellation coverage, larger ionospheric effects,  
 512 and multipath interference. The National Security Implications of Climate Change for U.S.  
 513 Naval Forces ([National Research Council, 2011](#)) details some of the limitations of the Global  
 514 Positioning System (GPS) at polar latitudes. Radio infrastructure that provides position  
 515 corrections and references does not regularly extend to polar regions. The effect is minor for  
 516 surface platform navigation —roughly 15 m of horizontal precision has been displayed at the  
 517 North Pole—but is significant enough to register against the modem’s detected travel times.

518 Fig. 13 zooms in on the GNSS and OWTT noise relative to the ice movement for two pairs  
 519 of modem buoy connections. The two panels indicate the GPS drift as  $\delta R = \sqrt{\delta x^2 + \delta y^2}$   
 520 and temporal drift,  $\delta t$ , relative to the median OWTT recorded between the two modems.

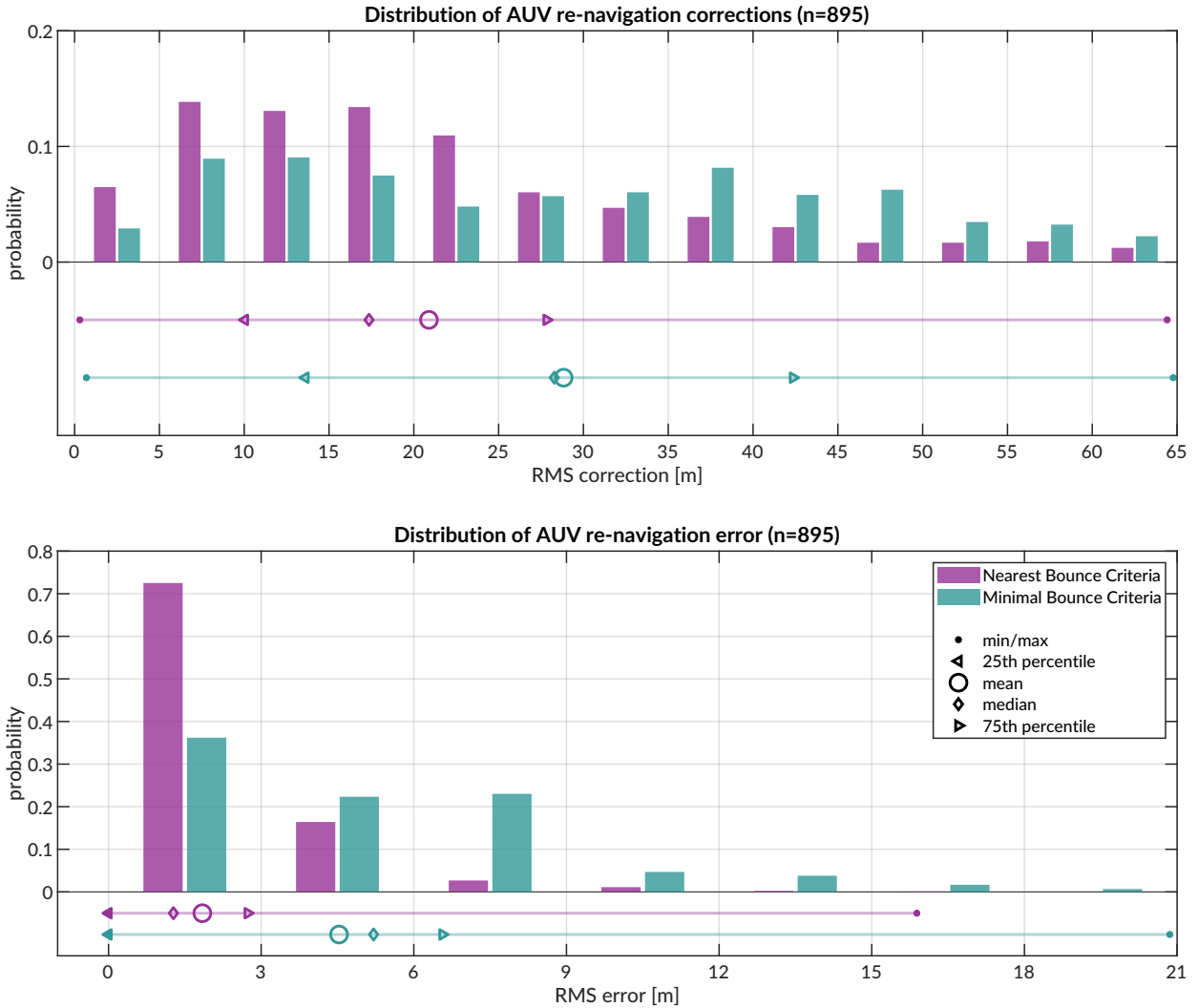


FIG. 12. Distribution of vehicle re-navigation corrections (top) and error (bottom) computed in post-processing for the Minimum and Nearest Bounce Criterion.

521 The dashed line is scaled by a group velocity of 1440 m/s, such that if there were ideal  
 522 sensor measurements with no drift, all events should exist on or near the line.

523 The top panel shows the connections between the North and East buoys. The clusters  
 524 scaling along the 1440 m/s guideline suggest relative ice movement picked up by both GNSS  
 525 and OWTT. But the vertical distribution across many arrival time bands is indicative of

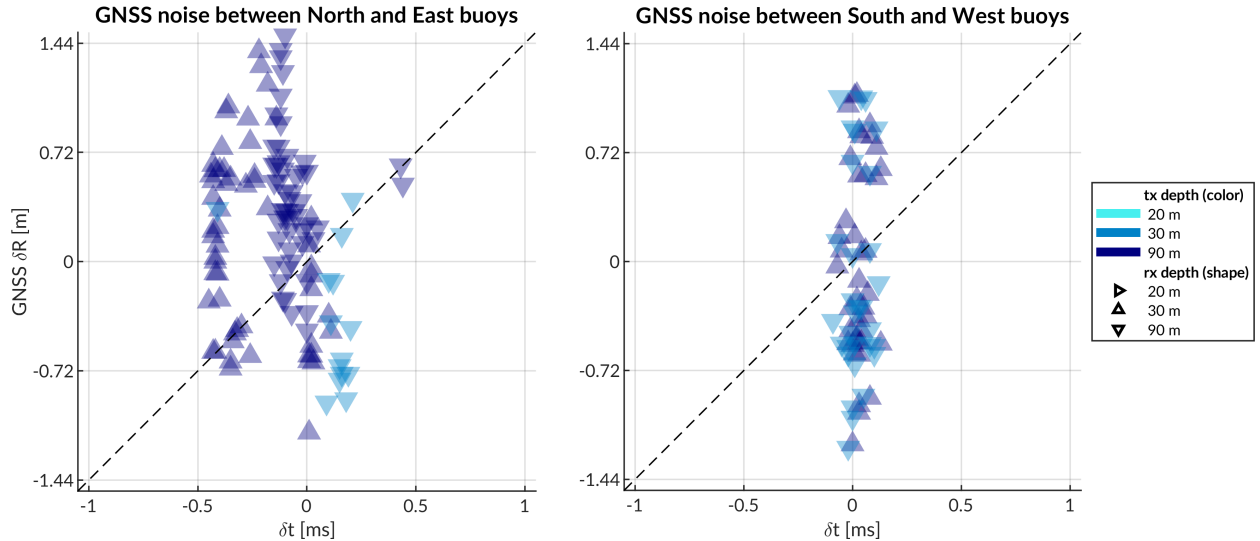


FIG. 13. A comparison of GPS drift (y-axis) versus OWTT drift (x-axis) for corners of the ICNN network with different source depths.

526 the GNSS fluctuations in precision, or noise. Some minor offsets between these vertical  
 527 bands relate to different operational configurations of source and receiver depth. The idea  
 528 of GNSS noise relative to OWTT is further indicated by events between two other buoys,  
 529 South and West. The relatively thin time window suggests these buoys are moving in  
 530 a more rigid ice floe and that there is minimal impact by source and receiver depth on  
 531 the spread of OWTT. Yet, the vertical distribution, spanning almost 4 meters, cannot be  
 532 explained by time differentials due to acoustic scattering, multipath, and/or environmental  
 533 microstructure. This conclusion corroborates the vertical spread of implied effective speeds  
 534 in Fig. 9.

535 **VI. DISCUSSION**

536 Underwater navigation research is broadly motivated by acquiring GNSS-like navi-  
 537 gation in GNSS-denied conditions. Accurate range estimation is essential to mitigating error.  
 538 Current approaches for underwater acoustic navigation simplify the non-linear relationship  
 539 between a SSP and timefronts with a deterministic sound speed. Thus, the conversion of  
 540 travel time into distance can be pre-conditioned for error and error growth over the course  
 541 of a vehicle mission. This work introduces a lightweight stochastic prediction of an effec-  
 542 tive sound speed along the path between source and receiver, retooling arrival methods  
 543 generally deemed too complex or labor intensive for real-time. We assume that the effec-  
 544 tive sound speed would be a locally smoothly varying function with respect to operational  
 545 conditions—horizontal and vertical differences and rate of difference between source and re-  
 546 ceiver. The field-tested approach, the minimal bounce criteria, facilitated a successful AUV  
 547 recovery in a total ice-covered, double ducted environment. The accuracy of the MBC was  
 548 validated against GPS-linked beacon-to-beacon communications. Given a consistent bias  
 549 towards overestimation, an improved algorithm, the nearest bounce criteria, was developed  
 550 on the insight that multipath structure may play an outsized role in maintaining a smoothly  
 551 varying effective sound speed. The NBC was developed with field data and reevaluated on  
 552 vehicle data, achieving a position accuracy and precision that rivals that of the deployed  
 553 GNSS puck.

554 A key insight for both approaches was seeking an eigenray ensemble around an estimated  
 555 location instead of seeking to unambiguously match arrivals. The ensemble diversified the

556 simulated multipath possibilities to better capture the actual multipath recorded. In this  
 557 way, the solution exploits multipath, generally viewed as a source of uncertainty, as a new  
 558 dimension of information to improve localization accuracy. Based on the navigation and re-  
 559 navigation results of our AUV deployment in the ice-covered Beaufort Sea, we conclude that  
 560 embedding a model-aided prediction of the effective sound speed has an outsized benefit  
 561 to minimizing trilateration error, and that our approach sufficiently resolves the acoustic  
 562 timefronts for an unpredictable, complex propagation environment like the double ducted  
 563 Beaufort Lens.

564 There are many avenues through which this approach can be further refined and tested for  
 565 field operations. Amongst them is defining the uncertainty grid for BELLHOP via stochastic  
 566 or data-driven measures such as the distance traveled by the AUV between ICNN updates  
 567 or the magnitude of the position corrections by the ICNN. Another is to entirely remove the  
 568 seeded range and instead rely on the submerged asset's depth and recorded OWTT to find  
 569 high probability fields in range.

570 The relatively simple nature of this approach suggests it is transferable to other envi-  
 571 ronments, spatio-temporal scales, and platforms. While it is likely a particular quirk of  
 572 the Beaufort Lens that filtering for reflection alone can produce a horizontal effective speed  
 573 that compensates for ray refraction and reflection, it is trivial to filter along other ways, like  
 574 number of turning points, to create a more diverse and informed set of multipath timefronts.  
 575 Though the majority of re-navigation results are within single-meter accuracy, future work  
 576 can examine how constellations of more LBL beacons can extend the operational domain  
 577 without adding an undesirable amount of error. One possibility is that, during a mission,

578 ICNN-like LBL implementations use a comparison of the GNSS self-position and acoustic po-  
579 sitioning to invert for the ocean volume, linking how vertical and horizontal sound speed  
580 structure impact transmission integrity. A fast tomographic estimate ([Deffenbaugh \*et al.\*, 1997](#);  
581 [Elisseeff \*et al.\*, 2002](#)), along with its uncertainty, can be continuously communicated to  
582 assets underway to maintain contact or enable adaptive sampling. In this sense navigation  
583 and tomography converge on the same set of component technologies—position estimation,  
584 sound speed parameterization estimation, ray path identification, and vehicle path optimiza-  
585 tion.

586 Spatio-temporal variability is a serious challenge for accurate real-time ranging. On  
587 one hand, the effectiveness of eigenray filtering algorithm is likely only challenged by the  
588 valid operational scales of a range independent propagation environment. Longer range  
589 experiments may provide more time for eigenray filtering. A bootstrapping approach that  
590 filters eigenrays for several randomly generated internal wave spectrums may compensate  
591 for otherwise unknowable spatio-temporal variability. The model-aided component to the  
592 eigenray filtering is compatible with vertical slices from any physically driven ocean model.  
593 But in the long run, more accurate and higher resolution global circulation models are  
594 needed to properly resolve features that alter ducted propagation at the scales discernible  
595 to an acoustic modem. Through-the-sensor methods can resolve local features but would  
596 require a degree of information sharing not readily supported on the acoustic channel for  
597 large scale variability. But addressing the spatial and temporal scales of what can be solved  
598 deterministically and what must be solved stochastically imposes a resolution constraint  
599 that is at odds with computational overhead for real-time operations. Resolving features

600 inaccurately, or with a false sense of confidence, could be more harmful than contextualizing  
601 the limitations of a range independent propagation over realistic bathymetry. Given that  
602 AUV operations are often on smaller spatial and temporal scales, the added benefit of a  
603 gridded model is quite small, and for features like the Beaufort Lens, not well resolved.

604 The methods presented in this paper, including the software projects ([Benjamin \*et al.\*, 2010](#);  
605 [Schneider \*et al.\*, 2015](#); [Schneider and Schmidt, 2010](#)), are open source and platform  
606 agnostic. Large AUVs, often large enough to support long duration and/or deep sea mis-  
607 sions, would benefit from including diurnal or tidal effects for ranging. Gliders, though  
608 generally low power and memory, have been equipped with acoustic modems. Their in-  
609 ability to maintain position within a region of reliable acoustic path makes the impact of  
610 an environmentally adaptive pseudorange estimation disproportionately positive. The ex-  
611 act adjustments to the ensemble eigenray filtering are predicated on the expected sound  
612 speed conditions and acoustic arrival structure; the problem is ripe application for other  
613 simulation testbeds or machine learning methods. The continued development of embed-  
614 ded acoustic processing on heterogenous platforms is fundamental to support a universal  
615 underwater navigation scheme comparable to GNSS.

616 **ACKNOWLEDGMENTS**

617 We acknowledge the significant operational effort spearheaded by the LAMSS ICEX20  
 618 team and all our collaborators. Bhatt was funded by a National Defense, Science, and  
 619 Engineering Graduate Fellowship. This work was supported by the Office of Naval Research  
 620 322-OA under ICEX20 (N00014-17-1-2474) and Task Force Ocean (N00014-19-1-2716).

621

622 Ballard, M. S., Badiey, M., Sagers, J. D., Colosi, J. A., Turgut, A., Pecknold, S., Lin,  
 623 Y.-T., Proshutinsky, A., Krishfield, R., Worcester, P. F., and Dzieciuch, M. A. (**2020**).

624 “Temporal and spatial dependence of a yearlong record of sound propagation from the  
 625 Canada Basin to the Chukchi Shelf,” The Journal of the Acoustical Society of America  
 626 **148**(3), 1663–1680, doi: [10.1121/10.0001970](https://doi.org/10.1121/10.0001970).

627 Barker, L. D., Jakuba, M. V., Bowen, A. D., German, C. R., Maksym, T., Mayer, L.,  
 628 Boetius, A., Dutrieux, P., and Whitcomb, L. L. (**2020**). “Scientific challenges and present  
 629 capabilities in underwater robotic vehicle design and navigation for oceanographic explo-  
 630 ration under-ice,” Remote Sensing **12**(16), 1–31, doi: [10.3390/RS12162588](https://doi.org/10.3390/RS12162588).

631 Bellingham, J. G., Leonard, J. J., Vaganay, J., Goudey, C. A., Atwood, D. K., Consi,  
 632 T. R., Bales, J. W., Schmidt, H., and Chrysostomidis, C. (**1995**). “AUV operations in  
 633 the Arctic,” in *Sea Ice Mechanics and Arctic Modeling Workshop*.

634 Benjamin, M. R., Schmidt, H., Newman, P. M., and Leonard, J. J. (**2010**). “Nested au-  
 635 tonomy for unmanned marine vehicles with MOOS-IvP,” Journal of Field Robotics **27**(6),

- 636 834–875, doi: [10.1002/rob.20370](https://doi.org/10.1002/rob.20370).
- 637 Bhatt, E. C. (2021). “A Virtual Ocean framework for environmentally adaptive, embed-  
638 ded acoustic navigation on autonomous underwater vehicles,” Ph.D. thesis, Woods Hole  
639 Oceanographic Institution, doi: [10.1575/1912/27309](https://doi.org/10.1575/1912/27309).
- 640 Bhatt, E. C., Howard, B., and Schmidt, H. (2022). “An Embedded Tactical Decision Aid  
641 Framework for Environmentally Adaptive Autonomous Underwater Vehicle and Commu-  
642 nication,” IEEE Journal of Oceanic Engineering (accepted).
- 643 Brooke, J. (1981). “ARCS (Autonomous remotely controlled submersible),” in *Proceedings  
644 of the 1981 2nd International Symposium on Unmanned Untethered Submersible Technol-  
645 ogy*, IEEE, Vol. 2, p. 28.
- 646 Chassignet, E. P., Hurlburt, H. E., Smedstad, O. M., Halliwell, G. R., Hogan, P. J.,  
647 Wallcraft, A. J., Baraille, R., and Bleck, R. (2007). “The HYCOM HYbrid Coordinate  
648 Ocean Model data assimilative system,” Journal of Marine Systems **65**(1), 60–83, doi:  
649 [10.1016/j.jmarsys.2005.09.016](https://doi.org/10.1016/j.jmarsys.2005.09.016).
- 650 Chen, R., Poulsen, A., and Schmidt, H. (2019). “Spectral, spatial, and temporal character-  
651 istics of underwater ambient noise in the {Beaufort} {Sea} in 1994 and 2016,” The Journal  
652 of the Acoustical Society of America **145**(2), 605–614, doi: [10.1121/1.5088601](https://doi.org/10.1121/1.5088601).
- 653 Chen, R., and Schmidt, H. (2020). “Temporal and spatial characteristics of the {Beaufort}  
654 {Sea} ambient noise environment,” The Journal of the Acoustical Society of America  
655 **148**(6), 3928–3941, doi: [10.1121/10.0002955](https://doi.org/10.1121/10.0002955).
- 656 Claus, B., Kepper, J. H., Suman, S., and Kinsey, J. C. (2018). “Closed-loop one-way-travel-  
657 time navigation using low-grade odometry for autonomous underwater vehicles,” Journal

- 658 of Field Robotics **35**(4), 421–434, doi: [10.1002/rob.21746](https://doi.org/10.1002/rob.21746).
- 659 Deffenbaugh, M., Bellingham, J. G., and Schmidt, H. (1996a). “The relationship between  
660 spherical and hyperbolic positioning,” in *OCEANS 96 MTS/IEEE Conference Proceedings.*  
661 *The Coastal Ocean - Prospects for the 21st Century*, Vol. 2, pp. 590–595, doi: [10.1109/OCEANS.1996.568293](https://doi.org/10.1109/OCEANS.1996.568293).
- 662
- 663 Deffenbaugh, M., Deffenbaugh, M., and Stanton, T. K. (1997). “Optimal {Ocean}  
664 {Acoustic} {Tomography} and {Navigation} with {Moving} {Sources},” {PhD} {thesis}.
- 665 Deffenbaugh, M., Schmidt, H., and Bellingham, J. G. (1996b). “Acoustic positioning in a  
666 fading multipath environment,” in *OCEANS 96 MTS/IEEE Conference Proceedings*, Vol.  
667 2, pp. 596—600, doi: [10.1109/OCEANS.1996.568294](https://doi.org/10.1109/OCEANS.1996.568294).
- 668 Duda, T. F., Morozov, A. K., Howe, B. M., Brown, M. G., Speer, K., Lazarevich, P.,  
669 Worcester, P. F., and Cornuelle, B. D. (2006). “Evaluation of a {Long}-{Range} {Joint}  
670 {Acoustic} {Navigation} / {Thermometry} {System},” in *{OCEANS} 2006*, pp. 1–6, doi:  
671 [10.1109/OCEANS.2006.306999](https://doi.org/10.1109/OCEANS.2006.306999).
- 672 Duda, T. F., Zhang, W. G., and Lin, Y.-T. (2021). “Effects of {Pacific} {Summer} {Water}  
673 layer variations and ice cover on {Beaufort} {Sea} underwater sound ducting,” *J. Acoust.  
674 Soc. Am.* 21.
- 675 Duda, T. F., Zhang, W. G., Lin, Y.-T., and Newhall, A. E. (2019). “Long-range sound  
676 propagation in the {Canada} {Basin},” .
- 677 Elisseeff, P., Schmidt, H., and Xu, W. (2002). “Ocean acoustic tomography as a data  
678 assimilation problem,” *IEEE Journal of Oceanic Engineering* **27**(2), 275–282, doi: [10.1109/JOE.2002.1002482](https://doi.org/10.1109/JOE.2002.1002482).

- 680 Eustice, R. M., Whitcomb, L. L., Singh, H., and Grand, M. (2006). “Recent advances in  
681 synchronous-clock one-way-travel-time acoustic navigation,” in *Oceans 2006*, IEEE, pp.  
682 1–6, doi: [10.1109/OCEANS.2006.306931](https://doi.org/10.1109/OCEANS.2006.306931).
- 683 Eustice, R. M., Whitcomb, L. L., Singh, H., and Grund, M. (2007). “Experimental Results  
684 in Synchronous-Clock One-Way-Travel-Time Acoustic Navigation for Autonomous Under-  
685 water Vehicles,” in *Proceedings 2007 {IEEE} {International} {Conference} on {Robotics}*  
686 and *{Automation}*, pp. 4257–4264, doi: [10.1109/ROBOT.2007.364134](https://doi.org/10.1109/ROBOT.2007.364134).
- 687 Fossum, T. O., Norgren, P., Fer, I., Nilsen, F., Koenig, Z. C., and Ludvigsen, M. (2021).  
688 “Adaptive Sampling of Surface Fronts in the Arctic Using an Autonomous Underwater  
689 Vehicle,” *IEEE Journal of Oceanic Engineering* **46**(4), 1155–1164, doi: [10.1109/JOE.2021.3070912](https://doi.org/10.1109/JOE.2021.3070912).
- 690 Freitag, L., Ball, K., Partan, J., Koski, P., and Singh, S. (2016). “Long range acoustic com-  
691 munications and navigation in the Arctic,” in *OCEANS 2015 - MTS/IEEE Washington*,  
692 IEEE, pp. 1–5, doi: [10.23919/oceans.2015.7401956](https://doi.org/10.23919/oceans.2015.7401956).
- 693 Graupe, C. E., Van Uffelen, L. J., Webster, S. E., Worcester, P. F., and Dzieciuch, M. A.  
694 (2019). “Preliminary results for glider localization in the Beaufort Duct using broadband  
695 acoustic sources at long range,” in *OCEANS 2019 MTS/IEEE Seattle, OCEANS 2019*,  
696 IEEE, pp. 1–6, doi: [10.23919/OCEANS40490.2019.8962637](https://doi.org/10.23919/OCEANS40490.2019.8962637).
- 697 Hayes, D. R., and Morison, J. H. (2002). “Determining turbulent vertical velocity, and  
698 fluxes of heat and salt with an autonomous underwater vehicle,” *Journal of Atmospheric  
699 and Oceanic Technology* **19**(5), 759–779.

- 701 Howe, B. M., Miksis-Olds, J., Rehm, E., Sagen, H., Worcester, P. F., and Haralabus, G.  
702 (2019). “Observing the Oceans Acoustically,” *Frontiers in Marine Science* **6**(JUL), 1–22,  
703 doi: [10.3389/fmars.2019.00426](https://doi.org/10.3389/fmars.2019.00426).
- 704 Jackson, E. (1983). “Autonomous remotely controlled submersible {“ARCS”},” in *Pro-*  
705 *ceedings of the 1983 3rd International Symposium on Unmanned Untethered Submersible*  
706 *Technology*, IEEE, Vol. 3, pp. 77–88.
- 707 Jakuba, M. V., Roman, C. N., Singh, H., Murphy, C., Kunz, C., Willis, C., Sato, T.,  
708 and Sohn, R. A. (2008). “Long-baseline acoustic navigation for under-ice autonomous  
709 underwater vehicle operations,” *Journal of Field Robotics* **25**(11-12), 861–879, doi: <https://doi.org/10.1002/rob.20250>.
- 710
- 711 Kepper, J. H., Claus, B. C., and Kinsey, J. C. (2017). “MEMS IMU and One-Way-Travel-  
712 Time Navigation for Autonomous Underwater Vehicles,” in *Oceans 2017 - {Aberdeen}*,  
713 Aberdeen, UK.
- 714 Krishfield, R., Toole, J., Proshutinsky, A., and Timmermans, M. L. (2008). “Automated  
715 ice-tethered profilers for seawater observations under pack ice in all seasons,” *Journal of*  
716 *Atmospheric and Oceanic Technology* **25**(11), 2091–2105, doi: [10.1175/2008JTECH0587.1](https://doi.org/10.1175/2008JTECH0587.1).
- 717
- 718 Kukulya, A., Plueddemann, A., Austin, T., Stokey, R., Purcell, M., Allen, B., Littlefield, R.,  
719 Freitag, L., Koski, P., Gallimore, E., Kemp, J., Newhall, K., and Pietro, J. (2010). “Under-  
720 ice operations with a REMUS-100 AUV in the Arctic,” in *2010 IEEE/OES Autonomous*  
721 *Underwater Vehicles, AUV 2010*, IEEE, pp. 1–8, doi: [10.1109/AUV.2010.5779661](https://doi.org/10.1109/AUV.2010.5779661).

- 722 Kunz, C., Murphy, C., Camilli, R., Singh, H., Bailey, J., Eustice, R., Jakuba, M., Nakamura, K. I., Roman, C., Sato, T., Sohn, R. A., and Willis, C. (2008). “Deep sea underwater  
 723 robotic exploration in the ice-covered arctic ocean with AUVs,” in *2008 IEEE/RSJ International Conference on Intelligent Robots and Systems, IROS*, IEEE, pp. 3654–3660, doi:  
 724  
 725  
 726 [10.1109/IROS.2008.4651097](https://doi.org/10.1109/IROS.2008.4651097).
- 727 Light, R. D., and Morison, J. (1989). “The Autonomous Conductivity-Temperture Vehicle:  
 728 First in the Seashuttle Family of Autonomous Underwater Vehicle’s for Scientific Pay-  
 729 loads,” in *Proceedings OCEANS*, Vol. 3, pp. 793–798, doi: [10.1109/OCEANS.1989.586683](https://doi.org/10.1109/OCEANS.1989.586683).
- 730 Litvak, A. G. (2015). “Acoustics of the deepwater part of the Arctic Ocean and of Russia’s  
 731 Arctic shelf,” *Herald of the Russian Academy of Sciences* **85**(3), 239–250, doi: [10.1134/S1019331615030144](https://doi.org/10.1134/S1019331615030144).
- 732  
 733 Mikhalevsky, P. N., Sperry, B. J., Woolfe, K. F., Dzieciuch, M. A., and Worcester, P. F.  
 734 (2020). “Deep ocean long range underwater navigation,” *The Journal of the Acoustical  
 735 Society of America* **147**(4), 2365–2382, doi: [10.1121/10.0001081](https://doi.org/10.1121/10.0001081).
- 736 National Research Council (2011). *National Security Implications of Climate Change for  
 737 U.S. Naval Forces* (National Academies Press, Washington, D.C.).
- 738 Norgren, P., Lubbad, R., and Skjetne, R. (2014). “Unmanned underwater vehicles in Arctic  
 739 operations,” in *Proceedings of the 22nd IAHR International Symposium on Ice. Singapore*,  
 740 pp. 89–101.
- 741 Paull, L., Saeedi, S., Seto, M., and Li, H. (2014). *AUV Navigation and Localization: A  
 742 Review*, **39**, pp. 131–149.

- 743 Plueddemann, A. J., Kukulya, A. L., Stokey, R., and Freitag, L. (2012). “Autonomous  
 744 Underwater Vehicle Operations Beneath Coastal Sea Ice,” IEEE/ASME Transactions on  
 745 Mechatronics **17**(1), 54–64, doi: [10.1109/TMECH.2011.2174798](https://doi.org/10.1109/TMECH.2011.2174798).
- 746 Porter, M. B. (2011). “The bellhop manual and user’s guide: Preliminary draft,” .
- 747 Poulsen, A. J., and Schmidt, H. (2017). “Acoustic noise properties in the rapidly changing  
 748 Arctic Ocean,” Proceedings of Meetings on Acoustics (28), 1–10, doi: [10.1121/2.0000552](https://doi.org/10.1121/2.0000552).
- 749 Randeni, S., Schneider, T., and Schmidt, H. (2020). “Construction of a high-resolution  
 750 under-ice AUV navigation framework using a multidisciplinary virtual environment,” in  
 751 *2020 IEEE/OES Autonomous Underwater Vehicles Symposium, AUV 2020*, IEEE, pp.  
 752 1–7, doi: [10.1109/AUV50043.2020.9267950](https://doi.org/10.1109/AUV50043.2020.9267950).
- 753 Randeni, S., Schneider, T., Schmidt, H., Bhatt, E., and Viquez, O. (2021). “A high-  
 754 resolution AUV navigation framework with integrated communication and tracking for  
 755 under-ice deployments,” Field Robotics (in review).
- 756 Rossby, T., Dorson, D., and Fontaine, J. (1986). “The RAFOS System,” Journal of  
 757 Atmospheric and Oceanic Technology **3**(4), 672–679, doi: [10.1175/1520-0426\(1986\)003<0672:TRS>2.0.CO;2](https://doi.org/10.1175/1520-0426(1986)003<0672:TRS>2.0.CO;2).
- 758
- 759 Rypkema, N. R., Fischell, E. M., and Schmidt, H. (2017). “One-Way Travel-Time Inverted  
 760 Ultra-Short Baseline Localization for Low-Cost Autonomous Underwater Vehicles,” in *2017*  
 761 *IEEE International Conference on Robotics and Automation*, Singapore, pp. 4920–4926.
- 762 Schmidt, H., and Schneider, T. (2016). “Acoustic communication and navigation in the  
 763 new Arctic — A model case for environmental adaptation,” 2016 IEEE Third Underwa-  
 764 ter Communications and Networking Conference (UComms) 1–4, doi: [10.1109/UComms](https://doi.org/10.1109/UComms).

765 2016.7583469.

766 Schneider, T., Petillo, S., Schmidt, H., and Murphy, C. (2015). “The dynamic compact  
767 control language version 3,” in *OCEANS 2015-Genova*, IEEE, pp. 1–7.

768 Schneider, T., and Schmidt, H. (2010). “Unified command and control for heterogeneous  
769 marine sensing networks,” *Journal of Field Robotics* **27**(6), 876–889, doi: <https://doi.org/10.1002/rob.20346>.

771 Schneider, T., and Schmidt, H. (2018). “NETSIM: A Realtime Virtual Ocean Hardware-in-  
772 the-loop Acoustic Modem Network Simulator,” in *2018 Fourth Underwater Communica-*  
773 *tions and Networking Conference (UComms)*, IEEE, pp. 1–5, doi: <10.1109/UComms.2018.8493188>.

774 Schneider, T., Schmidt, H., and Randeni, S. (2021). “Self-Adapting Under-Ice Integrated  
775 Communications and Navigation Network,” 2021 Fifth Underwater Communications and  
776 Networking Conference (UComms) 1–5, doi: <10.1109/UComms50339.2021.9598012>.

778 Singh, S., Grand, M., Bingham, B., Eustice, R., Singh, H., and Freitag, L. (2006). “Un-  
779 derwater acoustic navigation with the WHOI Micro-Modem,” in *Oceans 2006*, IEEE, pp.  
780 1–4, doi: <10.1109/OCEANS.2006.306853>.

781 Timmermans, M.-L., and Winsor, P. (2013). “Scales of horizontal density structure in the  
782 Chukchi Sea surface layer,” *Continental Shelf Research* **52**, 39–45.

783 Toole, J., Krishfield, R., Timmermans, M.-L., and Proshutinsky, A. (2011). “The Ice-  
784 Tethered Profiler: Argo of the Arctic,” *Oceanography* **24**(3), 126–135, doi: <10.5670/oceanog.2011.64>.

- 786 Van Uffelen, L. J., Howe, B. M., Nosal, E. M., Carter, G. S., Worcester, P. F., and Dzieciuch, M. A. (2016). “Localization and subsurface position error estimation of gliders using broadband acoustic signals at long range,” IEEE Journal of Oceanic Engineering 41(3), 501–508, doi: [10.1109/JOE.2015.2479016](https://doi.org/10.1109/JOE.2015.2479016).
- 787  
788  
789  
790  
791  
792  
793  
794
- Van Uffelen, L. J., Nosal, E.-M., Howe, B. M., Carter, G. S., Worcester, P. F., Dzieciuch, M. A., Heaney, K. D., Campbell, R. L., and Cross, P. S. (2013). “Estimating uncertainty in subsurface glider position using transmissions from fixed acoustic tomography sources,” The Journal of the Acoustical Society of America 134(4), 3260–3271, doi: [10.1121/1.4818841](https://doi.org/10.1121/1.4818841).
- 795 Van Uffelen, L. J. V. (2021). “Global Positioning Systems: Over Land and Under Sea,” Acoustics Today 17(1), 9.
- 796  
797  
798  
799  
800
- Webster, S. E., Eustice, R. M., Singh, H., and Whitcomb, L. L. (2009). “Preliminary deep water results in single-beacon one-way-travel-time acoustic navigation for underwater vehicles,” in *2009 IEEE/RSJ International Conference on Intelligent Robots and Systems, IROS 2009*, IEEE, pp. 2053–2060, doi: [10.1109/IROS.2009.5354457](https://doi.org/10.1109/IROS.2009.5354457).
- 801 Webster, S. E., Eustice, R. M., Singh, H., and Whitcomb, L. L. (2012). “Advances in single-beacon one-way-travel-time acoustic navigation for underwater vehicles,” The International Journal of Robotics Research 31(8), 935–950, doi: [10.1177/0278364912446166](https://doi.org/10.1177/0278364912446166).
- 804 Webster, S. E., Freitag, L. E., Lee, C. M., and Gobat, J. I. (2015). “Towards real-time under-ice acoustic navigation at mesoscale ranges,” in *Proceedings - IEEE International Conference on Robotics and Automation*, IEEE, Vol. 2015-June, pp. 537–544, doi: [10.1109/ICRA.2015.7139231](https://doi.org/10.1109/ICRA.2015.7139231).
- 805  
806  
807

808 Wu, M., Barmin, M. P., Andrew, R. K., Weichman, P. B., White, A. W., Lavelly, E. M.,  
809 Dzieciuch, M. A., Mercer, J. A., Worcester, P. F., and Ritzwoller, M. H. (2019). “Deep  
810 water acoustic range estimation based on an ocean general circulation model: Application  
811 to PhilSea10 data,” The Journal of the Acoustical Society of America **146**(6), 4754–4773,  
812 doi: [10.1121/1.5138606](https://doi.org/10.1121/1.5138606).